

## The Dynamics of CrO-FeO Catalysts during the High Temperature Water-Gas Shift Reaction: Molecular Structures and Reactivity

Christopher J Keturakis, Minghui Zhu, Emma K. Gibson, Marco Daturi, Franklin (Feng) Tao, Anatoly I Frenkel, and Israel E. Wachs

ACS Catal., **Just Accepted Manuscript** • DOI: 10.1021/acscatal.6b01281 • Publication Date (Web): 13 Jun 2016

Downloaded from <http://pubs.acs.org> on June 14, 2016

### Just Accepted

"Just Accepted" manuscripts have been peer-reviewed and accepted for publication. They are posted online prior to technical editing, formatting for publication and author proofing. The American Chemical Society provides "Just Accepted" as a free service to the research community to expedite the dissemination of scientific material as soon as possible after acceptance. "Just Accepted" manuscripts appear in full in PDF format accompanied by an HTML abstract. "Just Accepted" manuscripts have been fully peer reviewed, but should not be considered the official version of record. They are accessible to all readers and citable by the Digital Object Identifier (DOI®). "Just Accepted" is an optional service offered to authors. Therefore, the "Just Accepted" Web site may not include all articles that will be published in the journal. After a manuscript is technically edited and formatted, it will be removed from the "Just Accepted" Web site and published as an ASAP article. Note that technical editing may introduce minor changes to the manuscript text and/or graphics which could affect content, and all legal disclaimers and ethical guidelines that apply to the journal pertain. ACS cannot be held responsible for errors or consequences arising from the use of information contained in these "Just Accepted" manuscripts.

# The Dynamics of CrO<sub>3</sub>-Fe<sub>2</sub>O<sub>3</sub> Catalysts during the High Temperature Water-Gas Shift Reaction: Molecular Structures and Reactivity

Christopher J. Keturakis<sup>a†\*</sup>, Minghui Zhu<sup>a</sup>, Emma K. Gibson<sup>b‡</sup>, Marco Daturi<sup>b</sup>, Franklin Tao<sup>c</sup>, Anatoly I. Frenkel<sup>d</sup>, and Israel E. Wachs<sup>a\*</sup>

<sup>a</sup>*Operando* Molecular Spectroscopy and Catalysis Laboratory, Chemical Engineering Department, Lehigh University, Bethlehem, PA 18015 USA

<sup>b</sup>Laboratoire Catalyse et Spectrochimie, ENSICAEN, Université de Caen, CNRS, 6 Bd Maréchal Juin, F-14050 Caen Cedex, France

<sup>c</sup>Department of Chemical & Petroleum Engineering, University of Kansas, Lawrence, KS, 66047, USA

<sup>d</sup>Department of Physics, Yeshiva University, New York, NY 10016, USA

† Current Address: Cummins Emission Solutions, Stoughton, WI 53589, USA

‡ Current Address: Department of Chemistry, University College London, London WC1E 6BT, UK

Corresponding Authors\*

Email: cjk@cummins.com (C.J.K.)

Email: iew0@lehigh.edu (I.E.W.)

**Keywords:** water-gas shift, operando, in situ, spectroscopy, metal oxide, isotope exchange, surface

## Abstract

A series of supported CrO<sub>3</sub>/Fe<sub>2</sub>O<sub>3</sub> catalysts were investigated for the high temperature water-gas shift (WGS) and reverse-WGS reactions and extensively characterized using *in situ* and *operando* IR, Raman and XAS spectroscopy during the high temperature WGS/RWGS reactions. The *in situ* spectroscopy examinations reveal that the initial oxidized catalysts contain surface dioxo (O=)<sub>2</sub>Cr<sup>+6</sup>O<sub>2</sub> species and a bulk Fe<sub>2</sub>O<sub>3</sub> phase containing some Cr<sup>3+</sup> substituted into the iron oxide bulk lattice. *Operando* spectroscopy studies during the high temperature WGS/RWGS reactions show that the catalyst transforms during reaction. The crystalline Fe<sub>2</sub>O<sub>3</sub> bulk phase becomes Fe<sub>3</sub>O<sub>4</sub> and surface dioxo (O=)<sub>2</sub>Cr<sup>+6</sup>O<sub>2</sub> species are reduced and mostly dissolve into the iron oxide bulk lattice. Consequently, the chromium-iron oxide catalyst surface is dominated by FeO<sub>x</sub> sites, but some minor reduced surface chromia sites are also retained. The Fe<sub>3-x</sub>Cr<sub>x</sub>O<sub>4</sub> solid solution stabilizes the iron oxide phase from reducing to metallic Fe<sup>0</sup> and imparts an enhanced surface area to the catalyst. Isotopic exchange studies with C<sup>16</sup>O<sub>2</sub>/H<sub>2</sub> → C<sup>18</sup>O<sub>2</sub>/H<sub>2</sub> isotopic switch directly show that the RWGS reaction proceeds via the redox mechanism and only O\* from the surface region of the chromium-iron oxide catalysts are involved in the RWGS reaction. The number of redox O\* sites were quantitatively determined with the isotope exchange measurements under appropriate WGS conditions and demonstrated that previous methods have undercounted the number of sites by nearly an order of magnitude. The TOF values suggest that only the redox O\* sites affiliated with iron oxide are catalytic active sites for WGS/RWGS, though a carbonate oxygen exchange mechanism was demonstrated to exist, and that chromia is only a

textural promoter that increases the number of catalytic active sites without any chemical promotion effect.

## 1. Introduction

Mixtures of carbon monoxide and hydrogen, “syngas” or “water-gas”, are encountered in many crucial industrial processes including the manufacturing of ammonia (Haber-Bosch Process), methanol, hydrogen (Steam Methane Reforming (SMR), Water-Gas Shift (WGS)), and hydrocarbons (Fischer-Tropsch (FT)).<sup>1-4</sup> Water-gas was used as a source of hydrogen for the Haber-Bosch process by converting H<sub>2</sub>O to H<sub>2</sub> and CO to CO<sub>2</sub> since CO was a catalyst poison and needed to be removed from the water-gas stream. In 1914, Bosch and Wild implemented an iron-chromium oxide catalyst that converted CO into CO<sub>2</sub>, an easily separable chemical, at 400-500°C.<sup>5</sup> This first popularized the use of the WGS reaction, Eq. 1, though the reaction was discovered more than a century earlier. Nearly the same iron-chromium oxide based catalyst is still used today industrially, but with the addition of small amounts of copper.



Catalysts for the WGS reaction are divided into several groups. Iron and chromium oxide based catalysts are used for the high temperature WGS (HTS) at 350-450°C and copper-zinc-aluminum oxide based catalysts are used for the low temperature WGS (LTS) at 190-250°C. Additionally, there has been research into medium temperature shift (MTS) catalysts and sulfur tolerant “sour gas” shift catalysts. There have been many recent advancements in our understanding of the LTS catalysts,<sup>2,6</sup> but HTS catalysts remain poorly understood and nearly unchanged in composition for industrial use. The water-gas shift reaction has been studied for over a century and several good reviews of the literature already exist. Newsome reviewed the catalysis literature up to 1980,<sup>4</sup> Rhodes *et al.* reviewed the literature up to 1995,<sup>1</sup> Ladebeck and Wagner provided a review up to 2003 with an emphasis on fuel cell applications,<sup>7</sup> Ratnasamy and Wagner reviewed recent developments up to 2009,<sup>2</sup> and Zhu and Wachs focused on iron-based catalyst research up to 2016.<sup>8</sup> In recent years, there has also been an interest in developing Cr-free iron oxide based HTS catalysts because of the toxicity of hexavalent chromium, but successful substitutes have still not been achieved.<sup>9</sup> This literature review will primarily focus on new characterization studies performed in the last two decades that provide new insights to the HTS chromium-iron oxide catalysts, but will also explore older, relevant publications if they contain additional insights.

### 1.1 Ambient and *Ex Situ* Characterization

It is well known that ambient and *ex situ* or post reaction characterization suffers from some fundamental problems, such as sample hydration, oxidation and hydrocarbon adsorption, which limit the usefulness of such data. It is now also well established that catalyst surfaces are dynamic under reaction conditions, a trait that cannot be fully appreciated and understood without *in situ* and *operando* spectroscopy analysis.<sup>10</sup> Ambient and *ex situ* characterization of the iron-chromium oxide HTS catalyst have been performed with many techniques including X-ray Diffraction (XRD), IR Spectroscopy, Electron Microscopy, X-ray Absorption Spectroscopy (XAS), X-ray Photoelectron Spectroscopy (XPS), and Mössbauer Spectroscopy.<sup>11-35</sup> Results of these studies have reached the following conclusions: 1) the fresh catalyst is a Fe<sub>2</sub>O<sub>3</sub> phase, typically either alpha or gamma depending on synthesis and calcination conditions, 2) both Cr<sup>3+</sup> and Cr<sup>6+</sup> exist in the fresh catalyst, 3) Cr<sup>3+</sup> is substituted preferentially into the iron oxide lattice octahedral sites (O<sub>h</sub>), but not tetrahedral sites (T<sub>d</sub>), 4) there is

some surface segregation of chromium, 5) the reduced catalyst contains  $\text{Fe}_3\text{O}_4$  (magnetite), and 6) discrete  $\text{Cr}_2\text{O}_3$  particles are present above  $\sim 14$  wt%  $\text{Cr}_2\text{O}_3/\text{Fe}_2\text{O}_3$ .

## 1.2 *In Situ* and *Operando* Spectroscopy Characterization

There have been extensive studies on iron oxides, especially *in situ* IR studies, due to the additional interest from the Fischer-Tropsch community.<sup>36-47</sup> Boudjemaa *et al.* performed *in situ* IR spectroscopy on unpromoted  $\text{Fe}_2\text{O}_3$  during the WGS at  $450^\circ\text{C}$ <sup>47</sup> and did not detect any surface reaction intermediates at this high temperature. Relevant surface intermediates such as formates and carbonates, however, are not expected to exist at this high temperature.<sup>36-42</sup> Busca and Lorenzelli examined the IR spectrum of a dehydrated  $\text{FeCrO}_3$  catalyst and noted that a  $\text{Cr}^{6+}=\text{O}$  band is present, but could not identify its origin.<sup>48</sup> *In situ* Mössbauer spectroscopy of iron oxide catalysts under gas mixtures with different oxyreduction potentials revealed that nonstoichiometric  $\text{Fe}_3\text{O}_4$  was formed and that the stoichiometry depended on the oxyreduction potential of the gas mixture.<sup>49,50</sup> Furthermore, the oxygen vacancy in the iron oxide was found to correlate with catalyst activity up to  $350^\circ\text{C}$ . *In situ* XRD measurements by Zanchet *et al.* confirmed the transformation of  $\text{Fe}_2\text{O}_3$  to  $\text{Fe}_3\text{O}_4$  during the HTS at  $350^\circ\text{C}$  and above.<sup>51</sup> Kendelwicz *et al.* performed *in situ* Ambient Pressure-XPS (AP-XPS) studies of room temperature water adsorption (partial pressures of  $10^{-9}$  to 2 torr) on  $\text{Fe}_3\text{O}_4$  and combined the results with density functional theory (DFT) calculations.<sup>52</sup> It was found that at the lower partial pressures,  $\leq 10^{-4} - 10^{-5}$  Torr, water does not dissociatively adsorb on the surface, except on defect sites, and progressive dissociation into surface hydroxyl species takes place between  $10^{-4}$  and  $10^{-2}$  Torr.

Only one *operando* spectroscopy characterization experiment has been performed on the HTS catalysts of iron oxide and chromium-iron oxides. The rather unique study by Patlolla *et al.* combines three spectroscopic techniques (XAS, XRD, and Raman spectroscopy) with simultaneous online mass spectrometry (MS) for product analysis.<sup>53</sup> The quality of the Raman spectroscopy probe was insufficient for collection of data at high temperatures, thus, only allowing the Raman data to be collected *in situ* before the HTS reaction and at room temperature *ex-situ* after cooling in the WGS mixture. *In situ* Raman spectroscopy indicated the presence of hydrated  $\text{CrO}_4^{2-}$  oxoanions before reaction and demonstrated their disappearance, interpreted as reduction, after reaction. Before reaction, both catalysts were a mixture of  $\gamma/\alpha\text{-Fe}_2\text{O}_3$  at elevated temperatures and only  $\gamma\text{-Fe}_2\text{O}_3$  after cooling to room temperature. The corresponding *operando* XRD measurements confirmed that the catalysts were  $\gamma\text{-Fe}_2\text{O}_3$  before reaction,  $\text{Fe}_3\text{O}_4$  during the reaction, and returned to  $\gamma\text{-Fe}_2\text{O}_3$  upon cooling to room temperature. The *operando* XAS Fe-K edge data demonstrated that the catalysts were in the  $\text{Fe}^{3+}$  oxidation state before reaction and were partially reduced during the HTS reaction, which is consistently with  $\text{Fe}_3\text{O}_4$  formation.

## 1.3 Catalytic Active Site and Reaction Mechanism

Research concerning the nature and strength of oxygen bonds of metal oxides and its correlation to catalytic activity has been a topic of interest for many decades.<sup>54-60</sup> The adsorption and relaxation kinetics of  $\text{CO}/\text{CO}_2$  and  $\text{H}_2/\text{H}_2\text{O}$  gas mixtures indicated that surface oxygen sites and vacancies were the adsorption sites for the WGS reactants and products and comprised of  $\sim 10\text{-}20\%$  of the BET surface area under the conditions studied (pressures  $< 40\text{kPa}$  or  $\sim 0.4\text{atm}$  and temperatures of  $\sim 340\text{-}400^\circ\text{C}$ ).<sup>12,57,58,61-65</sup> Recently, the idea of counting sites was revisited by Zhu and Wachs who used the  $\text{C}^{16}\text{O}_2/\text{H}_2 \rightleftharpoons \text{C}^{18}\text{O}_2/\text{H}_2$  isotope exchange to count the number of participating oxygen sites during reaction at more industrially relevant conditions (pressures of 1 atm and temperatures of  $\sim 330\text{-}400^\circ\text{C}$ ) followed by post-isotope exchange  $\text{H}_2$ -TPR to probe the total amount of exchanged oxygen. Their results indicated that the entire surface layer of the catalyst is participating in the reaction and that previous oxygen site

counting methods were significantly undercounting the number of participating sites by almost an order of magnitude and, consequently, reporting turnover frequencies an order of magnitude or greater.<sup>66</sup>

The reaction mechanism has been debated for many decades with kinetic equations based on a regenerative or associative mechanism having some quantitative differences, albeit small differences, from the overall reaction kinetics.<sup>2,4,12,58,61,67</sup> Furthermore, experimental proof exists for both mechanisms. Equilibrium and kinetic measurements of individual reactants/products or with CO<sub>2</sub>/CO and H<sub>2</sub>O/H<sub>2</sub> gas mixtures has indicated that the regenerative mechanism is the primary pathway for the HT-WGS reaction.<sup>12,55,57,61,62,64,65,67-69</sup> Many of these same experiments, however, suggest that a second pathway may also exist due to the discrepancies between model and experimental rates mentioned above.<sup>12,57,61,70</sup> Research has suggested both surface formate and carbonate species, with experimental evidence for carbonates coming from isotope exchanges.<sup>57,70-76</sup>

Paradigm shifts in the fundamental understanding of heterogeneous catalysts have occurred since research on the chromium-iron oxide catalyst began over a century ago and it is now accepted that catalysts are dynamic during reaction and heterogeneous catalytic reactions only take place on the surface of solid catalysts. The absence of extensive fundamental *in situ* and *operando* spectroscopic studies of the surface of the Cr<sub>2</sub>O<sub>3</sub>/Fe<sub>2</sub>O<sub>3</sub> catalyst under appropriate HT-WGS conditions in the catalysis literature has hindered the development of molecular level insights about the catalytic active sites, surface reaction intermediates and the reaction mechanism. To address the surface properties of chromia-iron oxide catalysts during HT-WGS, a series of supported CrO<sub>3</sub>/Fe<sub>2</sub>O<sub>3</sub> catalysts were prepared and extensively characterized using *operando* Raman, IR, XAS and *in situ* AP-XPS spectroscopy. Potential surface reaction intermediates were examined with *in situ* IR spectroscopy during adsorption of probe molecules (CO, CO<sub>2</sub>, HCOOH, and CH<sub>3</sub>OH) and also monitored during the WGS reaction with *operando* IR spectroscopy. The redox characteristics of the chromium-iron oxide catalysts were determined by redox studies during *in situ* Raman and *operando* IR spectroscopy. The new fundamental insights allow development of structure-reactivity relationships for the high temperature WGS by supported CrO<sub>3</sub>/Fe<sub>2</sub>O<sub>3</sub> catalysts under realistic WGS conditions.

## 2. Experimental

### 2.1 Catalyst Synthesis and Preparation

The supported CrO<sub>3</sub>/Fe<sub>2</sub>O<sub>3</sub> catalysts were prepared by incipient wetness impregnation of aqueous solutions of chromium (III) nitrate (Cr(NO<sub>3</sub>)<sub>3</sub>•9H<sub>2</sub>O, Alfa Aesar, 98.5%) and distilled water on an iron oxide support (γ-Fe<sub>2</sub>O<sub>3</sub>, Alfa Aesar, 99+%), using an incipient-wetness point of ~0.4 mL/g of Fe<sub>2</sub>O<sub>3</sub> under ambient conditions. Samples were prepared with chromium oxide loadings of 1, 2, 3, 5, 7, and 9 wt% CrO<sub>3</sub>. The samples were allowed to dry overnight under ambient conditions, followed by a second drying step exposed to ambient air at 100°C for 4 hours in a programmable furnace (Thermolyne, Model 48000). Finally, the samples were subjected to calcination by ramping the temperature at 5°C/min under flowing air (Airgas, Zero grade) to 350°C for 2 hours. The final synthesized catalysts are denoted as x% CrO<sub>3</sub>/Fe<sub>2</sub>O<sub>3</sub>, where x = wt% of chromium oxide.

### 2.2 BET Specific Surface Area

The BET surface area of the catalyst samples was measured by nitrogen adsorption-desorption in flowing N<sub>2</sub> at -196 °C with a Quantasorb surface area analyzer (Quantachrome Corporation, Model OS-9). A sample quantity of ~0.3 g was typically employed for the measurement, and the sample was outgassed at 250 °C before N<sub>2</sub> adsorption (Quantachrome Corporation, Model QT-3).

### 2.3 In Situ FTIR Spectroscopy and Probe Molecules/Reactions

All FTIR studies on supported catalysts in §2.3 were performed at the University of Caen, France. For FTIR spectroscopy studies, the powdered catalyst samples were pressed into disks of ~10 mg/cm<sup>2</sup> and activated *in situ* in the IR quartz cell equipped with KBr windows and attached to a high vacuum

system.<sup>77</sup> Activation consisted of heating the catalyst at a rate of 10°C/min under 13 kPa of O<sub>2</sub> from room temperature (RT) to 350°C. The sample was held at 350°C for 45-60 mins followed by cell evacuation at the same temperature for 30 mins. The sample disk was moved from the furnace part of the cell to the optical section. Spectra were recorded at RT with a Nicolet Magna 550 FTIR spectrometer using 4 cm<sup>-1</sup> resolution and 128 scans. They were treated by the Nicolet OMNIC™ software. For the mixed metal oxide catalysts, Diffuse Reflectance FTIR (DRIFTS) was performed at Lehigh University in a Thermo Nicolet 8700 spectrometer equipped with a commercial Harrick High Temperature Reaction Chamber and Praying Mantis DRIFTS mirrors. The standard activation procedure is described below in §2.4.

### 2.3.1 Carbon Monoxide and Carbon Dioxide Probe Molecules

After catalyst activation in oxidizing conditions (10% O<sub>2</sub>/Ar (Airgas, certified, 10.00% O<sub>2</sub>/Ar balance)), liquid nitrogen was added to a jacket surrounding the reaction cell, except for optical windows, in order to cool the sample to -196°C (100K). For CO<sub>2</sub> adsorption, the jacket was, instead, filled with solid CO<sub>2</sub> to reach -78°C (195K). A glass bulb containing CO or CO<sub>2</sub> gas was attached to the vacuum system and incrementally dosed based on pressure gauges and a calibrated volume. The gas was introduced so the total partial pressure of CO or CO<sub>2</sub> in the cell was increased incrementally from 1 Torr to 100 Torr, with an IR spectrum taken at each increment. After 100 Torr was reached, an equilibrium partial pressure of CO or CO<sub>2</sub> between the glass bulb and cell was achieved, followed by the collection of another IR spectrum. After CO or CO<sub>2</sub> equilibration, the cell was evacuated to see if any species remained on the surface. If species remained on the surface of the catalyst then the temperature was increased, first to room temperature by allowing the liquid nitrogen or solid CO<sub>2</sub> to evaporate, then at 10°C/min until the surface species desorbed. Spectra were collected every 25 or 50°C.

### 2.3.2 Formic Acid and Methanol Probe Molecules

After catalyst activation in oxidizing conditions (10% O<sub>2</sub>/Ar (Airgas, certified, 10.00% O<sub>2</sub>/Ar balance)), a glass bulb containing HCOOH or CH<sub>3</sub>OH was attached to the vacuum system and incrementally dosed based on pressure gauges. The gas was introduced so the total partial pressure of HCOOH or CH<sub>3</sub>OH in the cell was increased incrementally from 1 Torr to 100 Torr, with an IR spectrum taken at each increment. After 100 Torr was reached, an equilibrium partial pressure of HCOOH or CH<sub>3</sub>OH was allowed into the cell, followed by the collection of another IR spectrum. After HCOOH or CH<sub>3</sub>OH equilibration, the cell was evacuated to eliminate any physisorbed species on the surface. The catalyst temperature was ramped at 10°C/min until the chemisorbed species desorbed. Spectra were collected every 25 or 50°C.

## 2.4 *In Situ* Raman Spectroscopy

The Raman spectra of the chromium-iron oxide catalysts were obtained with a high resolution, dispersive Raman spectrometer system (Horiba-Jobin Yvon LabRam HR) equipped with three laser excitations (532, 442, and 325 nm). The visible laser at 442 nm (violet) and the UV laser at 325 nm (not visible) were generated by a He-Cd laser (Kimmon, model IK5751I-G). The lasers were focused on the samples with a confocal microscope equipped with a 50X long working distance objective (Olympus BX-30- LWD) for the visible lasers and 15X objective (OFR LMU- 15X-NUV) for the UV laser. The LabRam HR spectrometer was optimized for the best spectral resolution by employing a 900 grooves/mm grating (Horiba-Jobin Yvon 51093140HR) for the visible lasers and a 2400 grooves/mm grating (Horiba-Jobin Yvon HR) for the UV laser. The resolution for both gratings is ~1 cm<sup>-1</sup>. The Rayleigh scattered light was rejected with holographic notch filters (Kaiser Super Notch). The notch filter window cutoffs were ~100 cm<sup>-1</sup> ~300 cm<sup>-1</sup> with the visible lasers and UV laser, respectively. The scattered light, after removing the Rayleigh scattering, was directed into a UV-sensitive liquid N<sub>2</sub> cooled CCD detector

(Horiba-Jobin Yvon CCD-3000V). The calibration of each laser line was performed with an Hg lamp by adjusting the groove gratings to match the zero position and minimize the error of the linearity across the full Raman spectrum range. The Hg lines chosen to represent the 532, 442, and 325 nm lasers were 546.07, 441.6, and 365.02 nm, respectively. Additionally, wavenumber calibration of the Raman spectrograph was checked using the silicon line at  $520.7\text{ cm}^{-1}$ .

The catalyst samples, typically consisting of between 5 and 10 mg of loose powder, were placed in an environmentally controlled high-temperature cell reactor (Harrick High Temperature Reaction Chamber) containing a quartz window and O-ring seals that were cooled with flowing cooling water. The sample temperature was controlled by a temperature controller (Harrick ATC/low voltage temperature control unit), providing linear heating rates of over  $50^{\circ}\text{C}/\text{min}$  through a K-type thermocouple. The catalyst bed, however, was fitted with a second K-type thermocouple for cascade control. Typical reactor cell conditions were room temperature (RT) -  $400^{\circ}\text{C}$ ,  $10\text{-}20^{\circ}\text{C}/\text{min}$  heating and cooling rates, atmospheric pressure, and  $\sim 40\text{ sccm}$  gas flowrates metered by mass flow controllers (Brooks, Model 5850E series).

The protocol for obtaining *in situ* Raman spectra under an oxidizing ( $\text{O}_2/\text{Ar}$ ) environment was as follows. The sample was initially heated at a rate of  $10^{\circ}\text{C}/\text{min}$  in the *in situ* cell to  $350^{\circ}\text{C}$  and held for 45-60 min under flowing 10%  $\text{O}_2/\text{Ar}$  (Airgas, certified, 10.00%  $\text{O}_2/\text{Ar}$  balance). For the acquisition of the Raman spectra, only the laser angles parallel to the incident beam were allowed to hit the catalyst sample, where the accumulation was collected at 10 s/scan for 7 scans with a 200 micrometer size hole. The Raman spectra were collected with the 442 nm laser, due to known  $\text{CrO}_x$  resonance enhancement,<sup>78</sup> at  $350^{\circ}\text{C}$  and also at RT after dehydration under the oxidizing conditions.

## 2.5 Operando Raman Spectroscopy and In Situ Redox Cycles

The *reverse*-WGS (RWGS) was performed using the same Harrick High Temperature Reaction Chamber and all Raman spectra were collected with a 442 nm laser. The gaseous outlet from the flow-through fixed-bed reactor was heated to  $120^{\circ}\text{C}$  and connected to an online mass spectrometer (Varian, 1200L quadrupole). The online MS spectra were collected every 0.5s and  $m/e$  values 15-75 simultaneously monitored. The  $m/z$  values used to detect the reactants and products were  $m/z = 28$  ( $\text{CO}$ ),  $m/z = 44$  ( $\text{CO}_2$ ), and  $m/z = 18$  ( $\text{H}_2\text{O}$ ), with the  $\text{CO}$  signal corrected for  $\text{CO}_2$  cracking in the MS. The Raman spectra were collected under reaction conditions with the simultaneous MS analysis of the reaction product stream to constitute the *operando* spectroscopy experimental mode.

The catalysts underwent the same dehydration procedure as described in section 2.3. After dehydration, the catalysts were heated to  $400^{\circ}\text{C}$  at  $10^{\circ}\text{C}/\text{min}$ , still under the  $\text{O}_2/\text{Ar}$  environment. At  $400^{\circ}\text{C}$  and after a short inert flush (15 mins), a *reverse*-WGS feed of X%  $\text{H}_2/\text{Y}\%$   $\text{CO}_2/\text{Ar}$  flowing at 42 cc/min total was introduced into the reactor cell. Experiments were repeated with the same total flow rate but with  $\text{H}_2:\text{CO}_2$  ratios ranging from 0.5 to 4. Spectra accumulation consisted of 120 s/scan for 5 scans. Spectra were collected every 5 minutes for the first 10 minutes, then once every 20<sup>th</sup> subsequent minute. The samples were run for a minimum of 60 minutes.

To determine the redox capabilities of the samples, the catalyst were allowed to reach steady state during RWGS (typically 60-120 mins) before an inert flush was performed for 5 mins at  $400^{\circ}\text{C}$ . After the flush, a mixture of either 33%  $\text{CO}_2/\text{He}$  or 2.5%  $\text{H}_2\text{O}/\text{He}$  (bubbled) was sent through the reactor for 30 mins. Another inert flush was performed for 5 mins before finally introducing a 10%  $\text{O}_2/\text{Ar}$  gas mixture into the reactor at  $400^{\circ}\text{C}$  for another 60 mins to perform the final re-oxidation. Raman spectra were collected after each step.

## 2.6 Operando X-ray Absorption Spectroscopy (XAS)

The X-ray Absorption Spectroscopy (XAS) experiments were performed at Brookhaven National Laboratory (BNL) National Synchrotron Light Source (NSLS) beamline X19A. The Cr and Fe K-edge

XAS data were obtained in fluorescence mode, using a PIPS detector. The monochromator Si(111) crystals were detuned 30% to minimize harmonics. The powder samples were loaded in a 1.0 mm o.d. (0.9 mm i.d.) quartz capillary, known also as Clausen cell. An Omega thermocouple was inserted into the capillary and placed adjacent to and contacting the catalyst bed. The catalyst sample was heated by using a resistive heater placed under the catalyst bed. Temperature was controlled using an Eurotherm temperature controller, and gas flow into the cell was controlled by Brooks mass flow controllers. The catalyst was activated by flowing 10% O<sub>2</sub>/He at 30 cc/min flow rate and ramping the temperature to 350°C at 10°C/min heating rate, followed by annealing at 350°C for 45-60 mins. For the WGS reaction, the temperature was raised to 400°C and the WGS reaction mixture introduced into the cell by directing CO mixed with helium through a water bubbler before entering the reactor (resulting in ~3% H<sub>2</sub>O and H<sub>2</sub>O:CO ratio of 2:1). The data were then collected at 400°C during the WGS reaction mixture flow. Simultaneous online product analysis was done using a 0-100 amu quadrupole mass spectrometer (SRS). The WGS reaction was performed for ~90 mins or until the reaction appeared to reach steady state conversion. After reaction, the catalyst was typically cooled to 350°C under flowing 10% O<sub>2</sub>/He and held for ~30 mins before cooling to room temperature under the same atmosphere. Data were collected at 350°C and at room temperature. The Fe K-edge EXAFS data were corrected for self-absorption by comparing the data measured in the Clausen cell in ambient conditions and using tape samples measured in transmission mode and free from self-absorption distortion. This comparison allowed us to obtain the scaling factor that was later applied to all *operando* XAS spectra to correct for self-absorption effects.<sup>79</sup>

## 2.7 *In situ* Ambient Pressure X-ray Photoelectron Spectroscopy (AP-XPS)

AP-XPS studies were performed by Franklin Tao's group by using lab-based ambient pressure X-ray photoelectron spectrometer.<sup>80-82</sup> Monochromator Al K  $\alpha$  (Microfocus 600) made by Specs Surface Nano Analysis GmbH was used as the X-ray source. Energy analyzer is Phobios 150. The sample was introduced to the reaction cell of this system. The CO and water vapor were mixed before introduction to the reaction cell. The introduction of H<sub>2</sub>O (1 Torr) and CO (0.5 Torr) was confirmed with mass spectrometer installed on lens 1. Photoemission features of Fe 2p and Cr 2p were collected during WGS reaction as a function of temperature. Catalytic activity was confirmed by formation of H<sub>2</sub> and CO<sub>2</sub> reaction products with the online mass spectrometer.

## 2.8 C<sup>16</sup>O<sub>2</sub>/C<sup>18</sup>O<sub>2</sub> Isotope Exchange during RWGS

The C<sup>16</sup>O<sub>2</sub>/C<sup>18</sup>O<sub>2</sub> isotope exchange experiments were carried out in the Altamira Instruments system (AMI 200) reactor connected to Dymaxion Dycor mass spectrometer (DME200MS). About 20mg of catalyst was loaded into a quartz U-tube, and was dehydrated with 10% O<sub>2</sub>/Ar at 400°C. After dehydration, the iron-chromium oxide catalyst was first allowed to equilibrate under C<sup>16</sup>O<sub>2</sub>/H<sub>2</sub> reverse WGS reaction conditions (10ml/min C<sup>16</sup>O<sub>2</sub>, 10ml/min H<sub>2</sub>) at 330°C for 1 hour, then the catalyst was flushed by inert gas (20ml/min He) for 10 min followed by switch to isotopic reverse WGS reaction conditions (10ml/min C<sup>18</sup>O<sub>2</sub>, 10ml/min H<sub>2</sub>). The C<sup>16</sup>O<sub>2</sub>/C<sup>18</sup>O<sub>2</sub> isotope exchange was monitored with the online mass spectrometer by recording the evolution of H<sub>2</sub><sup>16</sup>O, H<sub>2</sub><sup>18</sup>O, C<sup>16</sup>O<sub>2</sub>, C<sup>16</sup>O<sup>18</sup>O and C<sup>18</sup>O<sub>2</sub> species (m/z=17, 19, 44, 46, 48). All mass spec signals were normalized to the same maximum and minimum intensity to observe their transient behavior.

## 3. Results

### 3.1 Characterization before WGS/RWGS Reactions



A suite of *in situ* spectroscopy techniques, IR, Raman, XANES, and XPS were used to characterize the molecular structure of the supported  $\text{CrO}_3/\text{Fe}_2\text{O}_3$  catalyst before reaction. In all experiments, the catalyst was pretreated at  $350^\circ\text{C}$  in an oxidizing environment, which is considered to be the before reaction state. All techniques (Supplemental information, §S2.1 and Figures S1-S4) indicate that the initial iron oxide phase is  $\text{Fe}_2\text{O}_3$  (*Raman*:  $\gamma\text{-Fe}_2\text{O}_3$  bands present, *IR*:  $\text{Fe}_2\text{O}_3$  bands present, *XANES*: Fe K-edge spectra match  $\text{Fe}_2\text{O}_3$  reference compound, *XPS*: Fe 2p region exhibits characteristic peaks, shoulders, and satellite peaks of  $\text{Fe}^{3+}$  from  $\text{Fe}_2\text{O}_3$ ). Additionally, *in situ* IR spectra (Figure S1) revealed strong bands at  $1008\text{ cm}^{-1}$  along with a shoulder at  $993\text{ cm}^{-1}$ . The corresponding *in situ* Raman spectroscopy (Figure S2) exhibits a band at  $997\text{ cm}^{-1}$ . The band at  $\sim 1008\text{ cm}^{-1}$  is assigned to  $\nu_{\text{as}}(\text{Cr}(\text{=O})_2)$  and the band at  $\sim 993\text{-}997\text{ cm}^{-1}$  is assigned to  $\nu_{\text{s}}(\text{Cr}(\text{=O})_2)$  vibrations of a surface dioxo  $(\text{O=})_2\text{CrO}_2$  species.<sup>78,83-85</sup> The Cr-free  $\text{Fe}_2\text{O}_3$  sample exhibits many surface hydroxyl vibrations and the titration of these hydroxyls with increasing chromia loading reveals that the surface  $(\text{O=})_2\text{CrO}_2$  species anchor by reacting with surface Fe-OH species. The surface hydroxyl titration suggests that  $\sim 3\%$   $\text{CrO}_3/\text{Fe}_2\text{O}_3$  is the surface  $\text{CrO}_x$  monolayer coverage, but the reappearance of some surface hydroxyls upon further addition of chromia above monolayer coverage suggests that the iron oxide surface is re-exposed (either from clustering of chromia on the surface or its dissolution into the bulk). The *in situ* Raman spectrum (Figure S2) also possess a band at  $842\text{ cm}^{-1}$  from the  $\nu(\text{Cr-O-Fe})$  bridging bond between the surface dioxo species and  $\text{Fe}_2\text{O}_3$  support.<sup>78</sup> A small, unlabeled band at  $571\text{ cm}^{-1}$  is present for the  $9\%$   $\text{CrO}_3/\text{Fe}_2\text{O}_3$  catalyst, and may indicate the presence of a minor amount of  $\text{Cr}_2\text{O}_3$  nanoparticles (expected sharp band at  $550\text{ cm}^{-1}$ ).<sup>78</sup> *In situ* XANES Cr K-edge spectra (Figure S3) reveal that the monolayer catalyst ( $3\%$   $\text{CrO}_3/\text{Fe}_2\text{O}_3$ ) almost exclusively possesses  $\text{Cr}^{6+}\text{O}_4$  from the intense XANES pre-edge peak, while the  $9\%$   $\text{CrO}_3/\text{Fe}_2\text{O}_3$  catalyst possesses a mixture of  $\text{Cr}^{6+}\text{O}_4$  and  $\text{Cr}^{3+}\text{O}_6$  based on reference compounds (see supporting information Figure S5 for reference compounds). The Cr 2p region of the *in situ* XPS spectra (Figure S4) exhibits a peak at  $\sim 578.7 \pm 0.2\text{ eV}$  from  $\text{Cr}^{6+} 2p_{3/2}$  electrons<sup>86,87</sup> and two major  $\text{Cr}^{3+} 2p_{3/2}$  peaks at  $576.6$  and  $575.6\text{ eV}$  similar to that of  $\text{Cr}_2\text{O}_3$ .<sup>87</sup> All *in situ* spectra and a detailed analysis of each band/peak is given in the supplemental section S2.1 and Figures S1- S4.

## 3.2 Probe Molecules and Reactions

### 3.2.1 *In Situ* IR for Adsorption of $\text{CO}_2$ , CO, and HCOOH

Adsorption of the WGS reactants/products  $\text{CO}_2$  and CO was investigated at low temperatures in an IR spectroscopy system while adsorption of formic acid (HCOOH) was investigated at elevated temperatures and the results are given in Figure S6, S7, and S8 of the supplementary information, respectively. The adsorption of  $\text{CO}_2$  on the  $\text{Fe}_2\text{O}_3$  support (Figure S6) initially exhibits bands characteristic of carboxylates, bicarbonates, bidentate carbonates, and bridged carbonates, but as the catalyst warms to room temperature bands from a minor amount of surface formates ( $\text{HCOO}^*$ ) appear. The supported  $3\%$   $\text{CrO}_3/\text{Fe}_2\text{O}_3$  catalyst does not exhibit any major bands from carbonates and as the catalyst warms strong bands from surface formates appear which interact with surface dioxo  $(\text{O=})_2\text{CrO}_2$  species. The IR spectra for carbon monoxide adsorption are presented in Figure S7 and reveal that CO primarily bonds weakly with surface hydroxyls indicating the presence of weak Brønsted sites (slightly more acidic than on silica).<sup>93,94</sup> Additionally, a small amount of CO reactively adsorbs forming carboxylate and carbonate species, as seen for  $\text{CO}_2$  adsorption, but the coordination of each is unknown due to poor definition of the IR bands. Corresponding *in situ* IR spectra for  $\text{CO}_2$  and CO adsorption on the bulk  $\text{Cr}_2\text{O}_3^*\text{Fe}_2\text{O}_3$  mixed metal oxide catalysts were not undertaken.

Given that surface formate is the most proposed surface reaction intermediate during the WGS reaction,<sup>1,2,4</sup> *in situ* adsorption of HCOOH was investigated in a temperature programmed IR

spectroscopy system to determine the coordination and thermal stability of surface formate species and the spectra are shown in Figure S8 (difference spectra). The Fe<sub>2</sub>O<sub>3</sub> catalyst exhibits several adsorbed species at 100°C: physisorbed HCOOH, two bidentate formates (bidentate-I and -II), and a monodentate formate with bands summarized in Table S1.<sup>38,95-98</sup> All surface formates decompose by 250°C. The supported 3% CrO<sub>3</sub>/Fe<sub>2</sub>O<sub>3</sub> (monolayer coverage) catalyst exhibits only one major surface bidentate formate species and a minor amount of surface monodentate formate. The bidentate formate is thermally stable on the catalyst surface until 325°C, while the monodentate formate desorbs by 250°C. The supported 9% CrO<sub>3</sub>/Fe<sub>2</sub>O<sub>3</sub> catalyst exhibits some bands from all four formates observed on the Fe<sub>2</sub>O<sub>3</sub> catalyst. The bidentate-I and -II formates decompose by 300°C, while the monodentate formate decomposes by 250°C. The negative band at 1008-1014 cm<sup>-1</sup> on all Cr containing catalysts indicates that adsorbed formates interact with the surface (O=)<sub>2</sub>CrO<sub>2</sub> species. Catalysts containing the Cr oxide promoter exhibited higher thermal stability of surface formates than pure Fe<sub>2</sub>O<sub>3</sub> and also preferred a bidentate formate coordination, which is the major species for the monolayer catalyst.

3.3 Characterization during and after the WGS/RWGS Reactions

3.3.1 BET Surface Area

The BET surface areas of the freshly calcined and used catalysts are indicated in Table 1. The addition of chromia to the catalysts only slightly decreases the initial surface area before reaction from ~88 to 82-84 m<sup>2</sup>/g. After the RWGS reaction, the surface area of the catalysts dramatically decreases. While the surface area of the Cr-free Fe<sub>2</sub>O<sub>3</sub> catalyst decreases by an order of magnitude, the addition of chromia to iron oxide stabilizes the surface area of the supported CrO<sub>3</sub>/Fe<sub>2</sub>O<sub>3</sub> catalysts (factors of 1.36x and 2.44x for 3% and 9% CrO<sub>3</sub>/Fe<sub>2</sub>O<sub>3</sub>, respectively).

3.3.2 Operando Raman Spectroscopy

To investigate the phase changes of the catalysts during reaction, Raman spectroscopy measurements were performed at 400°C with simultaneous gas phase monitoring using an online MS (*operando* spectroscopy methodology). The results during the RWGS with H<sub>2</sub>:CO<sub>2</sub> ratios ranging from 0.5 to 4 are presented in Figures S9, S10, and S11 of the supplementary information for Fe<sub>2</sub>O<sub>3</sub>, 3% CrO<sub>3</sub>/Fe<sub>2</sub>O<sub>3</sub>, and 9% CrO<sub>3</sub>/Fe<sub>2</sub>O<sub>3</sub> catalysts, respectively. The *operando* Raman spectra of the Fe<sub>2</sub>O<sub>3</sub> catalyst (Figure S9) indicate that the catalyst transitions from a Fe<sub>2</sub>O<sub>3</sub> phase to Fe<sub>3</sub>O<sub>4</sub> during the reaction, at all H<sub>2</sub>:CO<sub>2</sub> ratios tested, while the corresponding MS signal shows steady-state production of CO and H<sub>2</sub>O after 60 minutes, confirming the equilibrated state of the catalyst. The *operando* Raman spectra of the supported 3% and 9% CrO<sub>3</sub>/Fe<sub>2</sub>O<sub>3</sub> catalysts are shown in Figures S10 and S11, and indicate the same bulk iron oxide transformation. Furthermore, Raman bands for the surface (O=)<sub>2</sub>CrO<sub>2</sub> species are initially present at 835 [ $\nu(\text{Cr-O-Fe})$ ] and 996 cm<sup>-1</sup> [ $\nu_s(\text{Cr(=O)}_2)$ ], but disappear during the RWGS reaction suggesting that the surface chromia sites have altered and most likely became reduced. The same results are also observed for all examined H<sub>2</sub>:CO<sub>2</sub> ratios. These findings reveal that Fe<sub>3</sub>O<sub>4</sub> is also the main bulk iron

**Table 1:** BET surface areas of the supported CrO<sub>3</sub>/Fe<sub>2</sub>O<sub>3</sub> catalysts before and after the *reverse*-WGS (RWGS) reaction.

Catalyst	Before RWGS (m <sup>2</sup> /g)	After RWGS (m <sup>2</sup> /g)
Fe <sub>2</sub> O <sub>3</sub>	88.2	8.4
3% CrO <sub>3</sub> /Fe <sub>2</sub> O <sub>3</sub>	81.5	11
9% CrO <sub>3</sub> /Fe <sub>2</sub> O <sub>3</sub>	83.9	20.5

oxide phase present for all chromium-iron oxide catalysts during the RWGS reaction. A more detailed analysis of the data is given in the supplemental section S2.3.

### 3.3.3 Operando X-ray Absorption Spectroscopy (XAS)

The dynamics of the Fe and Cr bonding environments (Fe-X and Cr-X) and oxidation states during the WGS reaction were probed by XAS studies at 400°C (labeled WGS S.S.) with simultaneous monitoring of the gas phase using a RGA mass spec (*operando* spectroscopy methodology). The spectral results during WGS ( $\text{H}_2\text{O}:\text{CO} = 2$ ) for  $\text{Fe}_2\text{O}_3$  (Figure S12 in supplementary information), supported 3%  $\text{CrO}_3/\text{Fe}_2\text{O}_3$  (Figure 1), and supported 9%  $\text{CrO}_3/\text{Fe}_2\text{O}_3$  (Figure S13 in supplementary information) are presented in the respective figures.

The Fe K-Edge XANES spectra of iron oxide before, during, and after the WGS reaction are presented in Figure S12A of the supplementary information. The XANES spectrum before reaction (ambient and 350°C Ox) is consistent with  $\text{Fe}_2\text{O}_3$  bulk phase ( $\alpha$ ,  $\gamma$ , or their mixture) from the pre-edge feature and edge position (reference compounds given in Figure S14 of supplementary information).<sup>92,99</sup> After ~70 mins. of the WGS reaction (WGS S.S.), the XANES edge position significantly shifts to lower energy and the sharp pre-edge feature is absent. These XANES features are consistent with a zero-valent metallic iron as the dominant iron phase. Upon subsequent re-oxidation (350°C ReOx), the XANES edge position is not fully recovered indicating an irreversible change to the bulk iron phase and a lower

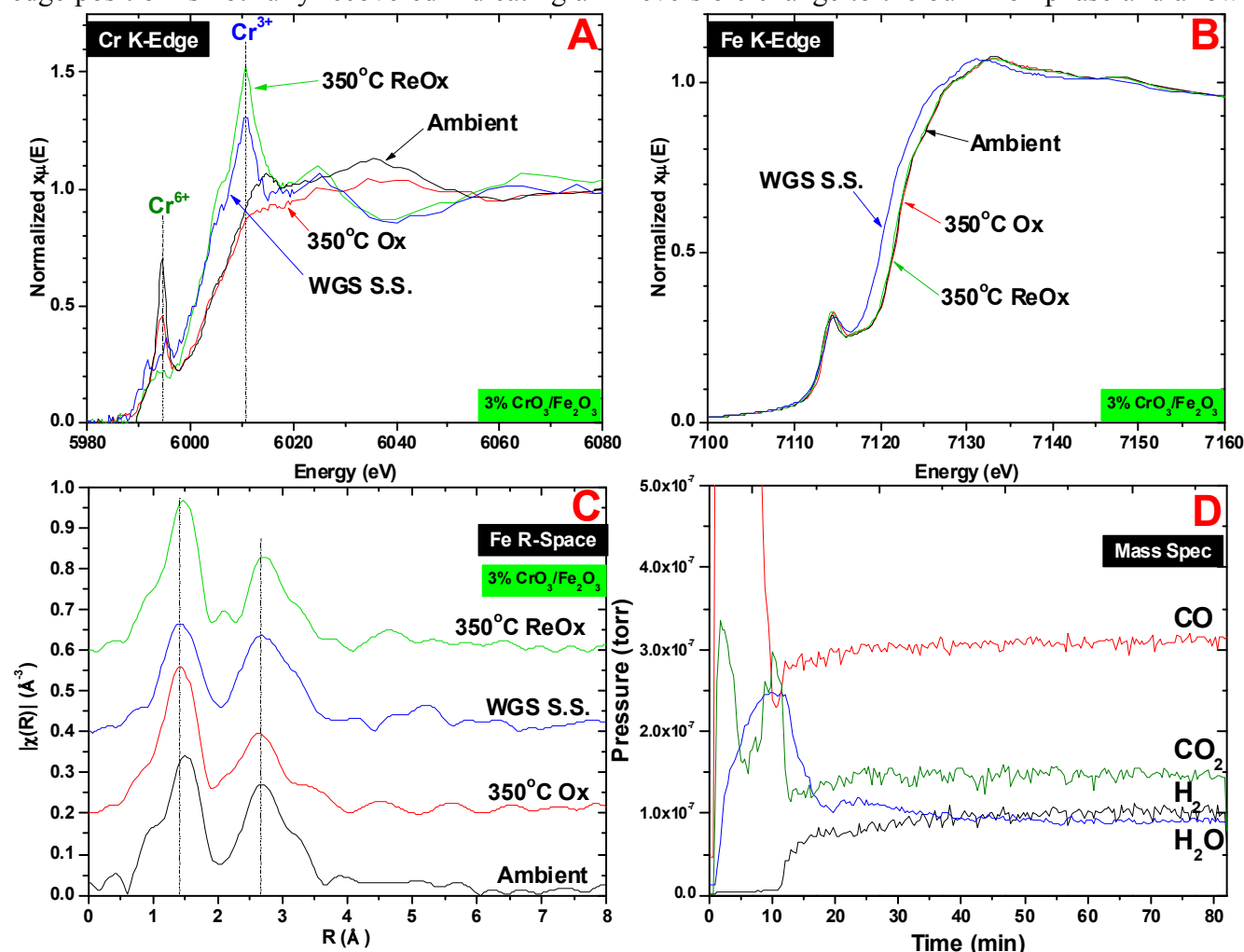


**Figure 1:** Operando XANES/EXAFS spectra of 3%  $\text{CrO}_3/\text{Fe}_2\text{O}_3$  at room temperature (ambient), before WGS (350°C Ox), during WGS at 400°C (WGS S.S.), and re-oxidized after WGS (350°C ReOx). A) XANES Cr K-edge spectra, B) XANES Fe K-edge spectra C) EXAFS Fe R-Space spectra, D) RGA data.

average oxidation state. The EXAFS data before reaction, Figure S12B of supplementary information, similarly suggests the presence of a  $\text{Fe}_2\text{O}_3$  bulk phase. The spectrum during reaction indicates a large fraction of zero-valent metallic iron exists, due to the appearance of a large Fe-Fe peak at  $\sim 1.8 \text{ \AA}$ , and a small fraction of an iron oxide phase, due to the low R peak at  $\sim 1.1 \text{ \AA}$  in the Fe-O bond region. The lack of high R peaks in the catalyst spectrum (high R peaks observed with the  $\text{Fe}^0$  reference compound) indicates an amorphous phase without long range order. After reaction, the EXAFS spectrum is not completely recovered upon re-oxidation, exhibiting a shift in the  $\text{Fe}^{\text{oct}}\text{-Fe}^{\text{oct}}$  peak (oct = octahedral coordination) and a broad shoulder between 1.5-2.0  $\text{ \AA}$ . The corresponding MS signal (Figure S12C of supplementary information) shows that steady state production of  $\text{CO}_2$  and  $\text{H}_2$  begins at  $\sim 70$  minutes, confirming that the WGS is occurring and that the XAS measurements were taken under steady state reaction conditions.

The Cr and Fe K-Edge XANES spectra for the supported 3%  $\text{CrO}_3/\text{Fe}_2\text{O}_3$  catalyst before, during and after the WGS reaction are presented in Figures 1A & 1B. Before reaction, the Cr K-Edge XANES pre-edge peak indicates that the catalyst possesses predominantly  $\text{Cr}^{6+}$ , which decreases in intensity upon heating to  $350^\circ\text{C}$  for pretreatment ( $350^\circ\text{C Ox}$ ). During reaction (WGS S.S.), the sharp pre-edge peak is lost, the edge shifts to lower energies, indicating the reduction of  $\text{Cr}^{6+}$  to  $\text{Cr}^{3+}$  (near edge peak at  $\sim 6011 \text{ eV}$  from  $\text{Cr}^{3+}$ ). After re-oxidation, the catalyst contains an even larger fraction of  $\text{Cr}^{3+}$ . A small bump at the  $\text{Cr}^{6+}$  pre-edge peak position during and after reaction may indicate that a small amount of  $\text{Cr}^{6+}$  is present. The Fe K-Edge XANES spectra before reaction (Figure 1B, ambient and  $350^\circ\text{C Ox}$ ) are consistent with an  $\text{Fe}_2\text{O}_3$  bulk phase, while the spectrum during reaction shifts to lower energies by  $\sim 1.5 \text{ eV}$ , which is consistent with an  $\text{Fe}_3\text{O}_4$  phase based on reference compounds (Figure S10 of supplementary information). The Fe K-edge position is recovered upon a post-reaction re-oxidation treatment indicating that the phase change is reversible. The EXAFS data before reaction, in Figure 1C, similarly suggests an  $\text{Fe}_2\text{O}_3$  phase, while the spectrum during reaction shows an increase in the  $\sim 3.2 \text{ \AA}$  shoulder from  $\text{Fe}^{\text{oct}}\text{-Fe}^{\text{tet}}$  bonds (tet = tetrahedral coordination), consistent with the cubic spinel structure of an  $\text{Fe}_3\text{O}_4$  phase. Post-reaction re-oxidation treatment recovers the original intensity of the  $\text{Fe}_2\text{O}_3$  peaks. The corresponding mass spec data in Figure 1D indicates that steady state production of  $\text{CO}_2$  and  $\text{H}_2$  begins at  $\sim 40$  mins, confirming that the XAS measurements were taken under steady state WGS reaction conditions. Results for the supported 9%  $\text{CrO}_3/\text{Fe}_2\text{O}_3$  catalyst, given in Figure S13 are qualitatively the same and provide the same conclusions.

### 3.3.5 *In situ* Ambient Pressure X-ray Photoelectron Spectroscopy (AP-XPS)

Evolution of the oxidation states of the catalyst atoms in the surface region (1-3 nm) during reaction were probed by *in situ* AP-XPS experiments performed at  $400^\circ\text{C}$ . Results from a WGS feed with a  $\text{H}_2\text{O}:\text{CO} = 2$  are given in Figure 2 and Figure S15 (supplementary information) for supported 3%  $\text{CrO}_3/\text{Fe}_2\text{O}_3$  and 9%  $\text{CrO}_3/\text{Fe}_2\text{O}_3$  catalysts, respectively. Initially, the Fe 2p region in Figure 2 (left,  $\text{O}_2$  treatment at  $350^\circ\text{C}$ ) is indicative of a  $\text{Fe}_2\text{O}_3$  phase, as previously discussed in §3.1.5. During reaction, the 719 eV satellite peak vanishes and the large  $\text{Fe}^{3+} 2p_{3/2}$  peak at  $\sim 710.8 \text{ eV}$  broadens. Likely, the broadening of the photoemission feature at  $\sim 710.8 \text{ eV}$  results from the appearance of a shoulder at 709-708 eV during reaction, which indicates the presence of  $\text{Fe}^{2+}$  in a  $\text{Fe}_3\text{O}_4$  or  $\text{FeO}$  phase, which is typically located at 708.4 eV.<sup>87</sup> As shown in Figure 2, the photoemission feature of Cr 2p region (right,  $\text{O}_2 350^\circ\text{C}$ ) reveals a contribution from  $\text{Cr}^{6+}$  (578.9 eV), with a fraction of 0.44, and  $\text{Cr}^{3+}$  (576.6 and 575.6 eV), with a fraction of 0.56, during pretreatment at  $350^\circ\text{C}$  in  $\text{O}_2$  before reaction, as previously discussed in §3.1.5. During reaction, the fraction of  $\text{Cr}^{6+}$  peak at 578.9 eV decreases as low as 0.27. In addition, the position of the main  $\text{Cr}^{3+}$  peaks shifts to 577.4/576.4 eV from 0-45 mins and then to 577.0/575.9 eV at 90 minutes. These peak shifts suggest that the local chemical environment of  $\text{Cr}^{3+}$  changes from  $\text{Cr}^{3+}$  solely coordinating with oxygen atoms to  $\text{Cr}^{3+}$  binding to lattice oxygen atoms and surface OH groups at 45 minutes, and then to  $\text{Cr}^{3+}$  in a chemical environment similar to  $\text{FeCr}_2\text{O}_4$  at 90 minutes.<sup>87</sup> Results for the

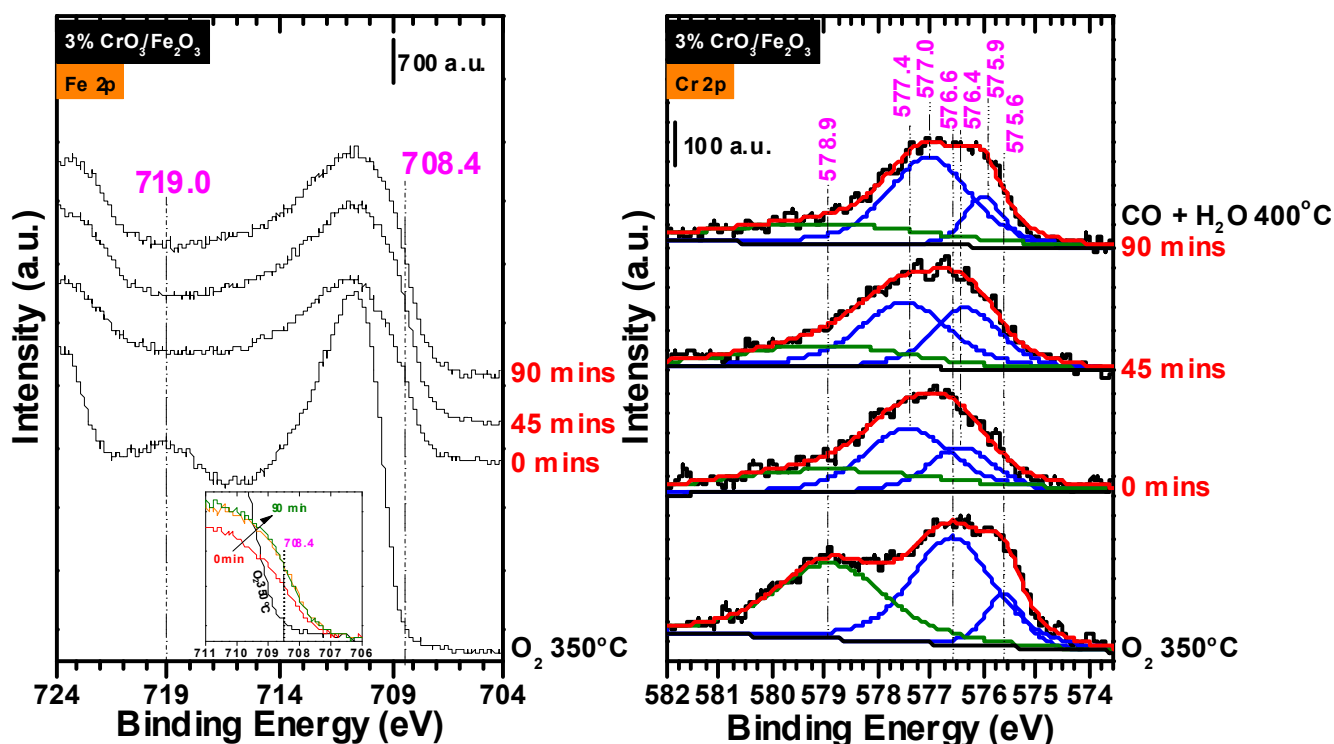


**Figure 2:** *In situ* NAP-XPS Fe 2p (left) and Cr 2p (right) spectra of 3% CrO<sub>3</sub>/Fe<sub>2</sub>O<sub>3</sub> during the WGS reaction at 400°C, 1.0 torr H<sub>2</sub>O and 0.5 torr CO. Fe 2p Inset: Zoomed region containing 708.4 eV shoulder.

supported 9% CrO<sub>3</sub>/Fe<sub>2</sub>O<sub>3</sub> catalyst, given in supplementary info Figure S15, are similar to the supported 3% CrO<sub>3</sub>/Fe<sub>2</sub>O<sub>3</sub> catalyst. The catalysts, however, differ in the extent of reduction of Fe<sub>2</sub>O<sub>3</sub> to the Fe<sub>3</sub>O<sub>4</sub> or FeO phase (reduction of the 3% CrO<sub>3</sub>/Fe<sub>2</sub>O<sub>3</sub> catalyst is much less than for the 9% CrO<sub>3</sub>/Fe<sub>2</sub>O<sub>3</sub> catalyst, which has a much smaller 708.4 eV shoulder). In addition, in the atomic fraction of Cr<sup>6+</sup> decreases to 0.21 during reaction for the supported 9% CrO<sub>3</sub>/Fe<sub>2</sub>O<sub>3</sub> catalyst.

### 3.3.5 *In situ* Raman Spectroscopy during Redox Cycles

After activating the supported 9% CrO<sub>3</sub>/Fe<sub>2</sub>O<sub>3</sub> catalyst in the RWGS reaction conditions, re-oxidation of the catalyst with H<sub>2</sub>O or CO<sub>2</sub> gases was investigated and the results are given in Figure 3. During the RWGS reaction, the catalyst transforms into the Fe<sub>3</sub>O<sub>4</sub> bulk phase (Raman bands at 279, 493, and 640 cm<sup>-1</sup>) and the surface chromia species (Raman band at ~997 cm<sup>-1</sup>) become reduced. After the RWGS, a feed of 2.5% H<sub>2</sub>O/He or 33% CO<sub>2</sub>/He was fed into the reactor to determine if either molecule can re-oxidize the bulk iron oxide phase and surface dioxo (O=)<sub>2</sub>Cr<sup>6+</sup>O<sub>2</sub> species. Under the H<sub>2</sub>O feed at 400°C (Figure 3A), a band from α-Fe<sub>2</sub>O<sub>3</sub> (215 cm<sup>-1</sup>) appears indicating that the bulk iron oxide phase was partially re-oxidized, but the Raman band for the surface dioxo (O=)<sub>2</sub>Cr<sup>6+</sup>O<sub>2</sub> species (993 cm<sup>-1</sup>), however, is not present. Upon exposure of the catalyst to CO<sub>2</sub> after the RWGS reaction at 400°C (Figure 3B), the surface dioxo (O=)<sub>2</sub>Cr<sup>6+</sup>O<sub>2</sub> species (997 cm<sup>-1</sup>) is again not present and bulk iron oxide bands from both Fe<sub>3</sub>O<sub>4</sub> (645 cm<sup>-1</sup>) and α-Fe<sub>2</sub>O<sub>3</sub> (214 cm<sup>-1</sup>) are present. The surface dioxo (O=)<sub>2</sub>Cr<sup>6+</sup>O<sub>2</sub> species (997 cm<sup>-1</sup>) are only partially recovered upon exposure to a 10% O<sub>2</sub>/Ar feed. Although H<sub>2</sub>O and CO<sub>2</sub> are sufficiently oxidizing for oxidation of the bulk Fe<sub>3</sub>O<sub>4</sub> phase to Fe<sub>2</sub>O<sub>3</sub>, both H<sub>2</sub>O and CO<sub>2</sub> are not sufficiently strong oxidizing agents for the re-oxidation of Cr<sup>+3</sup> present in WGS activated chromium-iron oxide catalysts back to Cr<sup>+6</sup>.

### 3.3.6 C<sup>16</sup>O<sub>2</sub>/C<sup>18</sup>O<sub>2</sub> Isotope Exchange during RWGS

The C<sup>16</sup>O<sub>2</sub>/C<sup>18</sup>O<sub>2</sub> isotope switching was performed with bulk Fe<sub>2</sub>O<sub>3</sub> and supported 3%, and 9% CrO<sub>3</sub>/Fe<sub>2</sub>O<sub>3</sub> catalysts during the RWGS reaction to gain insights into the oxygen exchange process

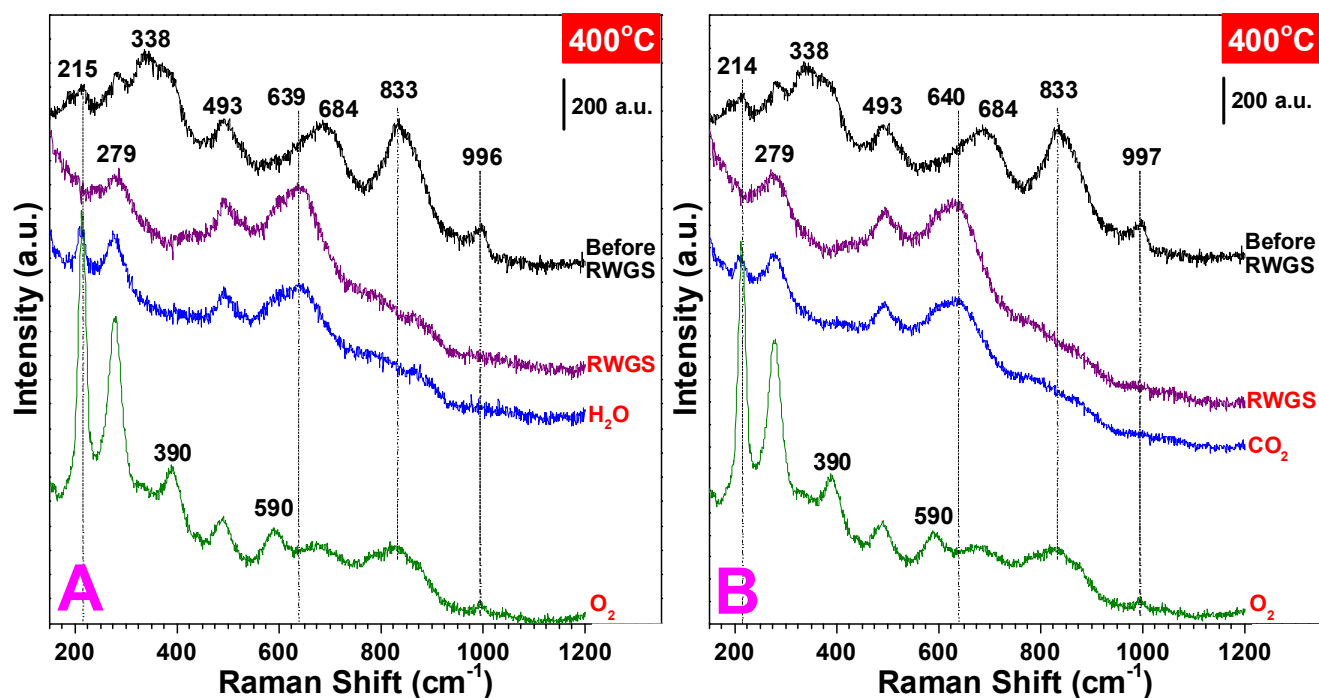


**Figure 3:** *In situ* Raman spectroscopy before, during, and after the RWGS reaction with a supported 9%  $\text{CrO}_3/\text{Fe}_2\text{O}_3$  catalyst. A) 2.5%  $\text{H}_2\text{O}/\text{Ar}$  oxidizing treatment after the RWGS reaction, B) 33%  $\text{CO}_2/\text{Ar}$  oxidizing treatment after the RWGS reaction.

taking place during the reaction and the results are presented in Figure 4. The catalysts were initially equilibrated under a typical RWGS feed, flushed with helium, and then exposed to an isotopic  $\text{H}_2+\text{C}^{18}\text{O}_2$  RWGS feed. For the bulk Cr-free iron oxide catalyst, after the  $\text{C}^{16}\text{O}_2/\text{C}^{18}\text{O}_2$  isotope switch, the first observable products were  $\text{C}^{16}\text{O}_2$  and  $\text{H}_2^{16}\text{O}$ , closely followed by the mixed oxygen  $\text{C}^{16}\text{O}^{18}\text{O}$  isotope (note that the transient CO isotope signals are not reliable because of  $\text{CO}_2$  cracking in the MS). The isotopic product  $\text{H}_2^{18}\text{O}$  is formed last. The transient production and decay of  $\text{C}^{16}\text{O}_2$  and  $\text{C}^{16}\text{O}^{18}\text{O}$  are similar while only the production of the water  $\text{H}_2^{16}\text{O}$  is similar. The complete decays of the  $\text{C}^{16}\text{O}_2$  and  $\text{C}^{16}\text{O}^{18}\text{O}$  isotopes are rapid, < 2 mins after exchange, compared to  $\text{H}_2^{16}\text{O}$ , ~5 mins after exchange.

The  $\text{C}^{16}\text{O}_2/\text{C}^{18}\text{O}_2$  isotope exchange experiment during RWGS reveals that the amount of  $^{16}\text{O}$  being supplied by the lattice of the iron-chromium oxide catalyst ( $\text{C}^{16}\text{O}^{18}\text{O}$ ,  $\text{H}_2^{16}\text{O}$ ,  $\text{C}^{16}\text{O}_2$  as well as undetectable  $\text{C}^{16}\text{O}$ ) is finite and small since most of the oxygen exchange occurs within ~2 mins. The number of  $^{16}\text{O}^*$  atoms participating during the  $\text{C}^{16}\text{O}_2/\text{C}^{18}\text{O}_2$  isotope exchange experiment were quantified by integration of the signals of  $^{16}\text{O}$ -containing products (sum of  $2*\text{C}^{16}\text{O}_2$ ,  $\text{C}^{18}\text{O}^{16}\text{O}$  and  $\text{H}_2^{16}\text{O}$ ). The RWGS activity and turnover frequencies based on a surface  $\text{O}^*$  as the most abundant reactive intermediate (MARI) are presented in Table 2. The overall catalyst activity ( $\text{H}_2\text{O mol}/(\text{g-s})$ ) is virtually the same with or without the addition of chromia to iron oxide, however, the number of participating  $^{16}\text{O}$  atoms ( $N_s = \text{O atoms/g}$ ) increases by 2.4. The corresponding TOF values ( $\text{TOF}=\text{activity}/N_s$ ) indicate that the specific TOF value for chromium-iron oxide catalyst is the same as the Cr-free iron oxide catalyst up to the initial monolayer coverage (3%  $\text{CrO}_3/\text{Fe}_2\text{O}_3$ ), after which additional chromium causes a decrease in the TOF by a factor of ~2.3. Thus, Cr is a textural promoter that increases the number of catalytic active sites, but does not chemically promote the WGS reaction by iron oxide. The slightly lower TOF for the 9%  $\text{CrO}_3/\text{Fe}_2\text{O}_3$  catalyst may indicate a slight retardation of the specific activity in the presence of significant chromia.



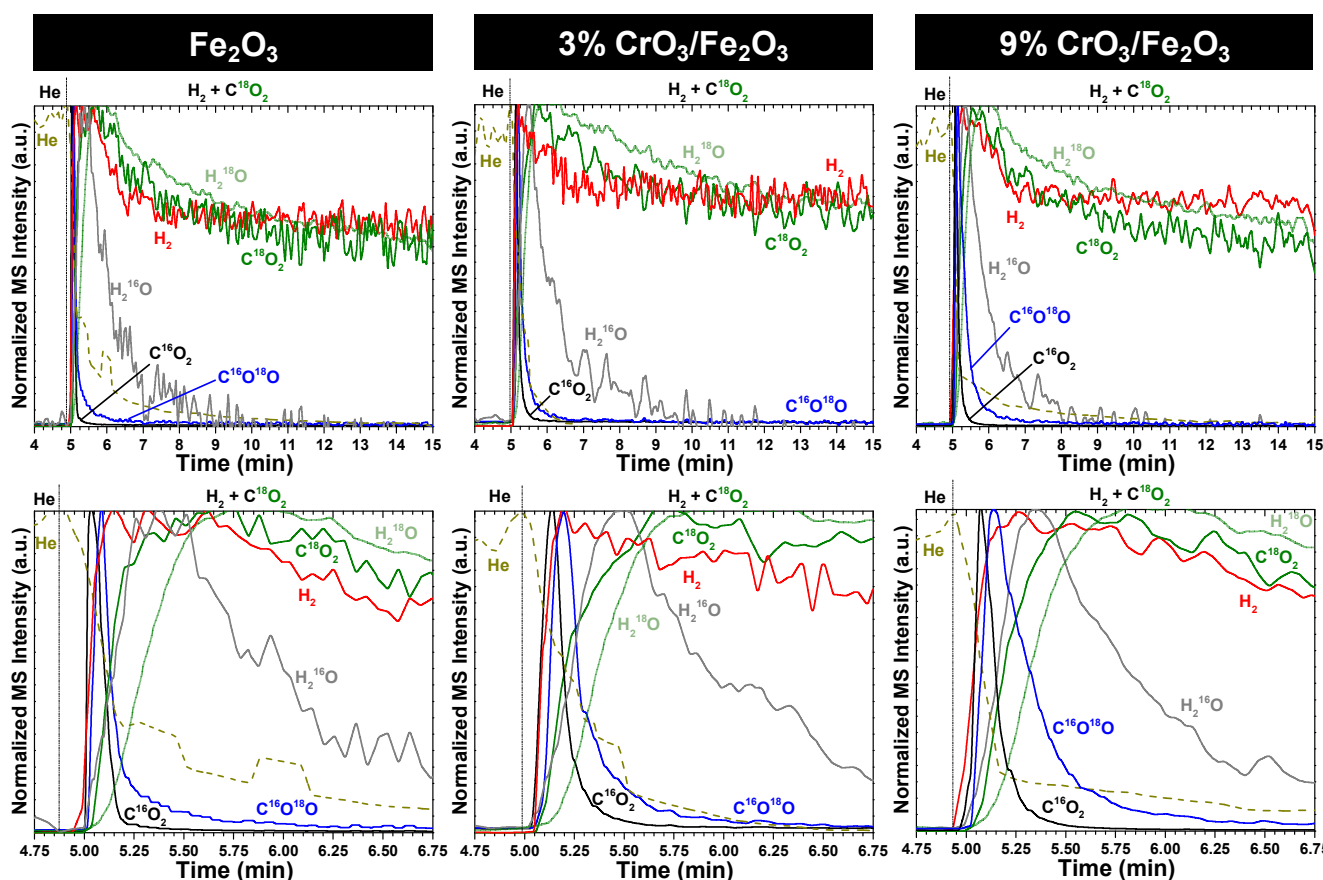


**Figure 4:** RWGS  $C^{16}O_2/C^{18}O_2$  isotope exchange with  $Fe_2O_3$  and  $x\%$   $CrO_3/Fe_2O_3$  supported catalysts. Top Row) Normalized MS signals, Bottom Row) Zoomed in region.

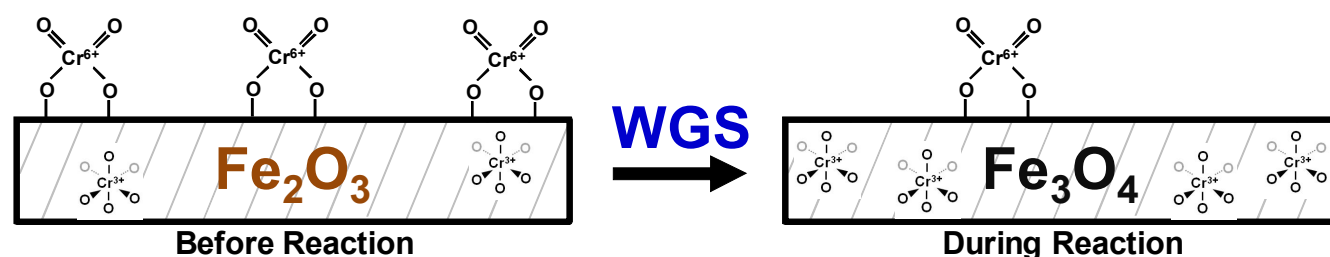
## 4. Discussion

### 4.1 Catalyst Structures in Initial Oxidized Catalyst

**4.1.1 Bulk Structures.** The bulk iron oxide phase is initially present as  $Fe_2O_3$  for all catalysts. For the supported  $CrO_3/Fe_2O_3$  catalysts, the iron oxide phase was present only as  $\gamma$ - $Fe_2O_3$  (see Figure S2), however, for pure iron oxide the phase can be a mixture of  $\alpha$ - and  $\gamma$ - $Fe_2O_3$ . The absence of discrete  $Cr_2O_3$  nanoparticles for most chromium oxide loadings greater than monolayer coverage for the supported  $CrO_3/Fe_2O_3$  catalysts (see Figure S2) suggests Cr dissolution into the  $Fe_2O_3$  support. This is further supported by the significant amount of  $Cr^{3+}$  present in the *in situ* XANES and XPS (Figures S3 and S4) of the supported 9%  $CrO_3/Fe_2O_3$  catalyst, but not of the *in situ* XANES for the monolayer supported 3%  $CrO_3/Fe_2O_3$  catalyst. In addition, just heating chromium-iron oxide catalysts under oxidizing conditions increases the concentration of  $Cr^{3+}$  in the bulk  $Fe_2O_3$  lattice (see Figure 1). Dissolution of chromium oxide into the iron oxide bulk lattice as  $Cr^{3+}$  is known to displace  $Fe^{2+}/Fe^{3+}$ .

**Table 2.** RWGS activity, number of sites [Ns:  $n(^{16}O)$ ], density of sites, and turnover frequencies (TOFs).

Catalyst	RWGS Activity ( $\times 10^{-6}$ mol/s·g)	Ns: $n(^{16}O)$ ( $\times 10^{-3}$ mol/g)	Density of Ns ( $^{16}O$ atoms/nm $^2$ )	TOF ( $\times 10^{-3}$ s $^{-1}$ )
$Fe_2O_3$	5.5	1.0	7	5.5
3% $CrO_3/Fe_2O_3$	6.0	1.1	8	5.4
9% $CrO_3/Fe_2O_3$	5.6	2.4	17	2.3



**Scheme 1:** Diagram of the surface and bulk molecule structures of the supported  $\text{CrO}_3/\text{Fe}_2\text{O}_3$  catalyst before and during the WGS reaction.

from octahedral sites and expose the iron oxide surface.<sup>11,13-17</sup> A diagram of the bulk structure of the initial oxidized chromium-iron oxide catalyst is given in Scheme 1.

**4.1.2 Surface Structures.** The initial oxidized chromium-iron oxide catalysts possess a surface chromia phase primarily present as dioxo  $(\text{O}=\text{O})_2\text{Cr}^{6+}\text{O}_2$  surface species, but a small amount of surface mono-oxo  $\text{O}=\text{CrO}_4$  species are also present (see Figure S1). The separation of  $\sim 14\text{ cm}^{-1}$  between the symmetric and asymmetric vibrations of  $\text{O}=\text{Cr}=\text{O}$  observed in the Raman and IR spectra, respectively, also matches the vibrational rules for dioxo metal oxides.<sup>11,13-17,100,101</sup> The surface chromia species on  $\text{Fe}_2\text{O}_3$  are metastable since their total concentration decreases at elevated temperatures in oxidizing environments (see Figure 1). There appears to be an equilibrium ratio of  $\text{Cr}^{6+}/\text{Cr}^{3+}$  in the surface region as indicated by nearly identical atomic fractions observed in the *in situ* XPS (Figure S4). The surface chromia species anchor to the surface of  $\text{Fe}_2\text{O}_3$  by titrating the iron oxide surface hydroxyls (see Figure S1). A diagram of the major surface chromia species on iron oxide before reaction is given in Scheme 1.

## 4.2 Catalyst Structures during the WGS/RWGS Reactions

**4.2.1 Bulk Structures.** During the WGS/RWGS reactions, the thermodynamically stable  $\text{Fe}_3\text{O}_4$  bulk phase is present in all chromium-iron oxide catalysts (see Figures 1, S9-S13, S15), even under very reducing conditions (Raman,  $\text{H}_2:\text{CO}_2 = 4$  for RWGS). For the Cr-free iron oxide catalyst, the metallic  $\text{Fe}^0$  bulk phase predominates (EXAFS, see Figure S12). This over-reduction of iron oxide is well-known in the literature, indicating the need for very careful catalyst activation.<sup>1,2,4</sup> The presence of  $\text{Cr}^{+3}$  in the bulk iron oxide lattice retards the formation of metallic  $\text{Fe}^0$  (EXAFS, see Figures 1, S12 and S13). The dissolution of  $\text{Cr}^{+3}$  into the iron oxide bulk lattice at elevated temperatures and WGS/RWGS reaction conditions is indicated by the increased  $\text{Cr}^{+3}$  signal (EXAFS, see Figure 1). Re-oxidation with  $\text{O}_2$  after RWGS only partially reoxidizes the chromia to surface  $\text{Cr}^{+6}$  (EXAFS and Raman, see Figures 1, 3, S13), and is consistent with the trapping of  $\text{Cr}^{+3}$  in the iron oxide bulk lattice.<sup>11,13-17</sup> The  $\text{Cr}^{+3}$  sites in the iron oxide bulk lattice during the WGS/RWGS reactions are responsible for stabilization of the  $\text{Fe}_3\text{O}_4$  phase (minimization of metallic  $\text{Fe}^0$  phase) and the enhanced BET surface area (see Table 1). A diagram of the bulk structures of the chromium-iron oxide catalysts during the WGS/RWGS reactions is given in Scheme 1.

**4.2.2 Surface Structures.** The surface of chromium-iron oxide catalysts during WGS/RWGS contains both exposed Cr and Fe sites. Although most of the chromia is dissolved as  $\text{Cr}^{+3}$  in the  $\text{Fe}_3\text{O}_4$  bulk lattice during WGS/RWGS, a small amount of  $\text{Cr}^{+6}$  also remains on the surface of the catalyst (see Figure 2). The Raman band for the dioxo surface  $\text{Cr}^{+6}$  species ( $997\text{ cm}^{-1}$ ) reappears, but with a low intensity, after the RWGS reaction by re-oxidation with  $\text{O}_2$  indicating the presence of some reduced  $\text{Cr}^{+3}$  species either on the topmost surface or in the surface region (several nm depth) of the chromium-iron oxide catalyst during the WGS/RWGS reactions. The minor amount of surface chromia species on the chromium-iron oxide catalyst during the WGS/RWGS reactions suggests that the chromium-iron oxide surface is



dominated by the  $\text{Fe}_3\text{O}_4$  surface features of  $\text{Fe}^{+2}$  and  $\text{Fe}^{+3}$  in octahedral and tetrahedral coordinations (*in situ* XPS, Figures 2 and S15). A diagram of the surface structure of the chromium-iron oxide catalyst during the WGS/RWGS reactions is depicted in Scheme 1. For pure iron oxide, it is hypothesized that the fraction of  $\alpha$ - and  $\gamma$ - $\text{Fe}_2\text{O}_3$  phases before reaction will influence the reactivity of the catalyst as either phase may promote specific stoichiometries on the catalyst surface.

### 4.3 Catalytic Active Sites during the WGS/RWGS Reactions

Although the surface of the chromium-iron oxide catalyst during the WGS/RWGS reactions contains mostly Fe and a minor amount of  $\text{Cr}^{+6}/\text{Cr}^{+3}$ , only the surface  $\text{FeO}_x$  sites are involved in the redox cycle. The inability to re-oxidize the surface  $\text{Cr}^{+3}$  sites with both  $\text{H}_2\text{O}$  and  $\text{CO}_2$ , the oxidizing agents during the WGS/RWGS reactions, suggests that surface  $\text{Cr}^{+3}$  sites can't participate in the WGS/RWGS reactions (see Figure 3) while  $\text{Cr}^{+6}$  is a spectator and may even retard the catalytic activity slightly, as indicated by decreases in the TOF upon chromium addition (Table 2). This leaves only the surface  $\text{FeO}_x$  as being the catalytic active sites for the WGS/RWGS reactions since Fe is reoxidized by both  $\text{H}_2\text{O}$  and  $\text{CO}_2$  (see Figure 3) and Cr-free iron oxide is also able to perform the WGS/RWGS reactions.

The HT-WGS catalysis literature is conflicted about the role of chromium in the chromium-iron oxide catalysts. Traditionally, it was concluded that the only function of chromium is as a textural promoter to increase the surface area of iron oxide, but the promotion mechanism was not known.<sup>1,2,4,7,14,21-25</sup> Multiple mechanisms, however, have been proposed for Cr stabilization of iron oxide and its catalytic role: chromia forms discrete  $\text{Cr}_2\text{O}_3$  particles on  $\text{Fe}_3\text{O}_4$  preventing agglomeration of iron oxide,<sup>73,75</sup> enrichment of  $\text{Cr}^{+3}$  in the surface region is more thermodynamically stable than iron oxide and reduces ion diffusion and sintering effects,<sup>23</sup> dissolved  $\text{Cr}^{+3}$  occupies octahedral sites in the bulk  $\text{Fe}_3\text{O}_4$  lattice that prevent sintering by forcing bulk  $\text{FeO}_6$  sites to occupy bulk  $\text{FeO}_4$  sites,<sup>102</sup> the chromia redox cycle of  $\text{Cr}^{+3} \rightleftharpoons \text{Cr}^{+6}$  promotes the  $\text{Fe}^{+2} \rightleftharpoons \text{Fe}^{+3}$  redox cycle of the  $\text{Fe}_3\text{O}_4$  phase.<sup>19</sup> The proposal that the  $\text{Cr}^{+3} \rightleftharpoons \text{Cr}^{+6}$  redox cycle promotes the  $\text{Fe}^{+2} \rightleftharpoons \text{Fe}^{+3}$  redox cycle of the  $\text{Fe}_3\text{O}_4$  phase is not supported by the current findings since the chromia redox cycle doesn't operate during the WGS/RWGS reactions (see Figure 3). The current Raman studies also demonstrate that discrete  $\text{Cr}_2\text{O}_3$  particles are not present on  $\text{Fe}_3\text{O}_4$  because of facile dissolution of  $\text{Cr}^{+3}$  in the iron oxide bulk lattice (see Figures S2, S9-S11), and negate this anti-agglomeration proposal. Analogously, a significant surface enriched chromia phase is not present during reaction and, thus, surface chromia probably can't be responsible for preventing sintering of iron oxide. The only stabilization mechanism consistent with the experimental findings is that dissolved  $\text{Cr}^{+3}$  occupies octahedral sites in the bulk  $\text{Fe}_3\text{O}_4$  lattice which prevent sintering by forcing bulk  $\text{FeO}_6$  sites to occupy bulk  $\text{FeO}_4$  sites. The current *operando* EXAFS findings (see Figures 1, S12, and S13) also reveal that the  $\text{Cr}^{+3}$  species dissolved in the iron oxide bulk lattice suppress formation of metallic  $\text{Fe}^0$  that is more prone to sintering than iron oxides.

The isotope switch experiment (Figure 4) provides quantification of the number of exchangeable active  $\text{O}^*$  atoms participating in the RWGS reaction under realistic reaction conditions and using the same reaction gas composition as for the *in situ/operando* spectroscopy experiments. Previous efforts utilized adsorption and relaxation kinetics of  $\text{CO}/\text{CO}_2$  and  $\text{H}_2/\text{H}_2\text{O}$  gas mixtures to quantify the number of  $\text{O}^*$  atoms and concluded that they comprised of ~10-20% of the surface area under the conditions studied (pressures < 40kPa or ~0.4atm and temperatures of ~340-400°C).<sup>12,57,58,61-65</sup> It has been demonstrated that the  $\text{Fe}_3\text{O}_4$  (111) surface possess  $\frac{3}{4}$  monolayer of oxygen atoms (14.2 atoms/ $\text{nm}^2$ ) and  $\frac{1}{4}$  monolayer of iron atoms that can be saturated with hydroxyls (4.7 atoms/ $\text{nm}^2$ ), which gives an overall density of 18.9 oxygen atoms/ $\text{nm}^2$ .<sup>103,104</sup> Results of the current isotope exchange give an experimental value ranging from 7-17  $^{16}\text{O}$  atoms/ $\text{nm}^2$ , indicating that nearly the entire surface layer can participate in the HT-WGS reaction and that previous methods have significantly undercounted the number of sites by nearly an order of magnitude. It is likely that undercounting in the literature is due to the use of high vacuum systems that can alter the catalyst surface with multiple evacuations, low pressures during

counting steps (< 40kPa), and the use of only half of the WGS reactants/products (CO/CO<sub>2</sub> or H<sub>2</sub>/H<sub>2</sub>O mixtures) during counting, which does not simulate the oxyreduction potential of the full WGS mixture.

#### 4.4 Surface Reaction Intermediates during the WGS/RWGS Reactions

There have been many surface reaction intermediates proposed for the WGS reaction with surface carbonates and formates being the most popular. Although surface intermediates have been observed for the low temperature WGS (Cu-Zn-Al) catalysts, there has been no direct evidence for surface reaction intermediates during the high temperature WGS/RWGS reactions,<sup>1,2,4</sup> only some indirect evidence of carbonates from isotopic (<sup>18</sup>O<sub>2</sub> and C<sup>18</sup>O<sub>2</sub>) temperature-programmed desorption experiments.<sup>57</sup> This is related to the short lifetime and low concentrations of the surface intermediates during high temperature WGS/RWGS that prevents their observation. For example, the efficient exchange of <sup>18</sup>O from C<sup>18</sup>O<sub>2</sub> with the chromium-iron oxide catalyst to form C<sup>16</sup>O<sub>2</sub> and C<sup>18</sup>O<sup>16</sup>O, as observed during isotope exchange (Figure 4), suggests that some exchange proceeds via surface carboxylate/carbonate intermediates, but these intermediates can only be detected spectroscopically at sub-ambient temperatures where they have a long lifetime (see Figure S6 and S7). Another possible reason for the lack of detection of surface intermediates during high temperature WGS/RWGS is the loss of transparency of the catalysts with respect to IR. Similarly, surface formate intermediates were observed on the iron and chromium-iron oxide catalysts upon adsorption of CO<sub>2</sub> (see Figure S6), HCOOH (see Figure S8) and CH<sub>3</sub>OH (see Figure S18), but at temperatures lower than those typically encountered for the high temperatures of ~400°C WGS/RWGS reactions since surface formates are not stable above 325 °C (see Figure S8). Even performing the WGS reaction at lower temperatures of 200-325°C does not yield the IR spectra of surface formate intermediates (see Figures S16 and S17). The lack of observation of surface reaction intermediates during high temperature WGS/RWGS are clouded by the possible loss of the IR signal from the chromium-iron oxide catalyst's reduced state. The most abundant reactive intermediate is actually the surface O\* sites on the catalysts as shown by the isotope exchange analysis.

#### 4.5 WGS/RWGS Reaction Mechanisms

Two reaction mechanisms have been proposed for the high temperature WGS/RWGS reactions: associative mechanism involving a surface reaction intermediate and a redox mechanism involving oxygen exchange between the gases and the iron oxide-based catalyst.<sup>1,2,4</sup> As already indicated, there is no direct evidence for the associative mechanism since surface intermediates are not detectable on either iron oxide or chromium-iron oxide catalysts during high temperature WGS/RWGS (see Figures S16 and S17). The associative mechanism may be operating during high temperature WGS/RWGS, but at present it hasn't be directly proven.

There is direct evidence, however, that the redox mechanism is operating during the high temperature RWGS reaction from transient C<sup>16</sup>O<sub>2</sub>/H<sub>2</sub> → inert flush → C<sup>18</sup>O<sub>2</sub>/H<sub>2</sub> experiments. The isotope switch experiments demonstrate that the RWGS reaction is proceeding via the redox mechanism since the isotope switch readily produces <sup>16</sup>O-containing reaction products (C<sup>16</sup>O<sub>2</sub>, C<sup>16</sup>O<sup>18</sup>O and H<sub>2</sub><sup>16</sup>O) in the C<sup>18</sup>O<sub>2</sub>/H<sub>2</sub> reaction environment and the exchange is nearly complete within 2 mins. The short exchange time indicates that a surface Mars-van Krevelen (MVK) reaction mechanism is taking place where only the surface layer is exchanging oxygen atoms, rather than a bulk MVK mechanism where complete exchange only occurs after an extended period of time. The formation of the C<sup>16</sup>O<sub>2</sub> and C<sup>16</sup>O<sup>18</sup>O products is not only from the RWGS since they can also form when only C<sup>18</sup>O<sub>2</sub> is exchanged with the equilibrated <sup>16</sup>O-containing catalyst. This suggests that the CO<sub>2</sub> exchange also takes place via short lived surface carboxylates/carbonates, which is a parallel oxygen exchange pathway.<sup>57</sup> Formation of H<sub>2</sub><sup>16</sup>O

before  $\text{H}_2^{18}\text{O}$  in the presence of  $\text{C}^{18}\text{O}_2/\text{H}_2$  is consistent with a redox process taking place during RWGS. Furthermore, the isotope switch experiment also provides quantification of the number of exchangeable active  $\text{O}^*$  atoms participating in the RWGS reaction under realistic reaction conditions.

#### 4.6 Structure-Activity Relationships

The catalytic active sites during the WGS/RWGS are  $\text{O}^*$  atoms affiliated with iron oxide sites in the outermost surface layer. This conclusion is supported by the (i) low concentration of surface chromia sites on the equilibrated chromium-iron oxide catalyst because of significant dissolution of  $\text{Cr}^{+3}$  into the iron oxide bulk lattice (see Figures 1-3, S2-S4, S9-S13, S15), (ii) ability of Cr-free iron oxide to perform HT-WGS/RWGS (see Figures 4, S9, S12), (iii) re-oxidation of  $\text{Fe}^{+2}$  to  $\text{Fe}^{+3}$  with  $\text{CO}_2$  and  $\text{H}_2\text{O}$  (see Figure 3), (iv) inability to reoxidize  $\text{Cr}^{+3}$  back to  $\text{Cr}^{+6}$  with  $\text{CO}_2$  and  $\text{H}_2\text{O}$  (see Figure 3), (v) inability to extensively re-oxidize  $\text{Cr}^{+3}$  back to surface  $\text{Cr}^{+6}$  even with  $\text{O}_2$  after WGS/RWGS due to its dissolution in the iron oxide bulk lattice (see Figures 1, 3, S13, S19-S20), and (vi) lack of increase and even slight decrease in TOF for Cr-promoted iron oxide catalysts (see Table 2). Thus, the only function of the chromia promoter is to stabilize the  $\text{Fe}_3\text{O}_4$  phase with a higher surface area (textural promoter), which is in agreement with the current accepted mechanism in the literature.

#### 5. Conclusions

A series of supported  $\text{CrO}_3/\text{Fe}_2\text{O}_3$  catalysts prepared by incipient wetness impregnation were investigated for the high temperature WGS reaction as a function of chromia loading and extensively characterized. Characterization before reaction by *in situ* IR, Raman, XAS, and AP-XPS revealed that the catalyst contains a 2-D surface phase consisting primarily of dioxo  $(\text{O}=\text{O})_2\text{Cr}^{+6}\text{O}_2$  species and a bulk  $\gamma\text{-Fe}_2\text{O}_3$  phase with some  $\text{Cr}^{+3}$  substituted into the bulk lattice. The adsorption of probe molecules was monitored using *in situ* IR spectroscopy and revealed various adsorbed carbonates and formates from CO and  $\text{CO}_2$  adsorption, and adsorbed formates from  $\text{HCOOH}$  adsorption directly. Surface formate species were thermodynamically preferred and were demonstrated to be stable up to  $250\text{-}325^\circ\text{C}$  on the catalyst surface.

Characterization during the high temperature WGS reaction by *operando* IR, Raman, XAS, and *in situ* AP-XPS revealed that crystalline  $\text{Fe}_3\text{O}_4$  phase is the active bulk phase and surface dioxo  $(\text{O}=\text{O})_2\text{Cr}^{+6}\text{O}_2$  species become reduced during reaction to  $\text{Cr}^{+3}$  and migrate into the bulk iron oxide lattice ( $\text{Fe}_{3-x}\text{Cr}_x\text{O}_4$ ). *In situ* AP-XPS data have revealed that a minor amount of  $\text{Cr}^{+6}$  species may remain on the catalyst surface under reaction conditions. Corresponding *in situ* Raman and *operando* IR redox cycles indicate that the trace surface  $\text{Cr}^{+6}$  is a spectator species during the WGS reaction. Isotope exchange experiments during the RWGS indicate a surface Mars-van Krevelen mechanism is occurring and the catalytic active sites during the WGS/RWGS are surface  $\text{O}^*$  atoms affiliated with iron oxide sites in the surface region. The chromia promoter only increases the population of sites and it does not chemically promote the reaction. Furthermore, quantification of the active  $\text{O}^*$  atoms indicates that previous titration methods have been undercounting the number of sites by nearly an order of magnitude. These new insights have led to a modern fundamental understanding of the high temperature WGS catalyst.

**Supporting Information Available:** Results available include 1) *in situ* IR and Raman spectroscopy, *in situ* XANES/EXAFS, and *in situ* XPS of the dehydrated catalyst, 2) XANES and EXAFS reference compounds, 3) *in situ* IR spectroscopy during adsorption of probe molecules CO,  $\text{CO}_2$ ,  $\text{HCOOH}$ , and  $\text{CH}_3\text{OH}$ , 4) *operando* Raman spectroscopy during the water-gas shift reaction, 5) *operando* XANES/EXAFS during the water-gas shift reaction, 6) *in situ* AP-XPS during the water-gas shift

reaction, 7) *operando* IR spectroscopy during the water-gas shift reaction, and 8) *operando* IR spectroscopy during redox cycles. This material is available free of charge via the Internet at <http://pubs.acs.org>.

## Acknowledgements

The authors gratefully acknowledge help of Relja Vasic and Nebojsa Marinkovic with synchrotron measurements at Brookhaven National Laboratory. CJK and IEW gratefully acknowledge support by the NSF IREE Award No. 0609018 and NSF Award No. 1511689. AIF acknowledges support by the U.S. DOE Grant No. DE-FG02-03ER15476. Beamline X19A of the NSLS is supported in part by the U.S. DOE Grant No. DE-FG02-05ER15688. NSLS is supported by U.S. DOE Contract No. DE-AC02-98CH10886. FT acknowledges support by the Chemical Sciences, Geosciences and Biosciences Division, Office of Basic Energy Sciences, Office of Science, U.S. Department of Energy under Grant No. DE-SC0014561.

## References

1. Rhodes, C.; Hutchings, G.; Ward, A. *Catal. Today* **1995**, *23*, 43-58.
2. Ratnasamy, C.; Wagner, J. P. *Catalysis Reviews* **2009**, *51*, 325-440.
3. Brenna, G. New Catalyst for the H<sub>2</sub> Production By Water-Gas Shift Reaction Processes, Università di Bologna, Italy, 2010.
4. Newsome, D. S. *Catal. Rev. -Sci. Eng.* **1980**, *21*, 275-318.
5. Bosch, C.; Wild, W. United States Patent 1,115,776, 1914.
6. Rodriguez, J. A.; Hanson, J. C.; Stacchiola, D.; Senanayake, S. D. *Phys. Chem. Chem. Phys.* **2013**, *15*, 12004-12025.
7. Ladebeck, J. R.; Wagner, J. P. In *Handbook of Fuel Cells – Fundamentals, Technology and Applications*; Vielstich, W., Lamm, A. and Gasteiger, H. A., Eds.; John Wiley & Sons: Chichester, 2003; Vol. 3, pp 190-201.
8. Zhu, M.; Wachs, I. E. *ACS Catalysis* **2016**, *6*, 722-732.
9. Lee, D. -.; Lee, M. S.; Lee, J. Y.; Kim, S.; Eom, H. -.; Moon, D. J.; Lee, K. -. *Catal. Today* **2013**, *210*, 2-9.
10. Wachs, I. E.; Keturakis, C. J. In *Comprehensive Inorganic Chemistry*; Schlögl, R., Ed.; Elsevier: Waltham, MA, 2013; Vol. 7, pp 131-151.
11. Filoti, G.; Nistor, L.; Doca, I.; Brasoveanu, I.; Spanu, V.; Teodorescu, V.; Rotaru, P.; Blejoiu, S. I. *Revue Roumaine de Chimie* **1979**, *24*, 1101-1105.

12. Kubsh, J. E.; Chen, Y.; Dumesic, J. A. *J. Catal.* **1981**, *71*, 192-200.
13. Kundu, M. L.; Sengupta, A. C.; Maiti, G. C.; Sen, B.; Ghosh, S. K.; Kuznetsov, V. I.; Kustova, G. N.; Yurchenko, E. N. *J. Catal.* **1988**, *112*, 375-383.
14. Pereira, A.; Berrocal, G.; Marchetti, S.; Alborno, A.; De Souza, A.; Rangel, M. *J. Mol. Catal. A: Chem.* **2008**, *281*, 66-72.
15. Reddy, G. K.; Gunasekera, K.; Boolchand, P.; Dong, J.; Smirniotis, P. G. *J. Phys. Chem. C* **2011**, *115*, 7586-7595.
16. Reddy, G. K.; Gunasekera, K.; Boolchand, P.; Smirniotis, P. G. *J. Phys. Chem. C* **2011**, *115*, 920-930.
17. Reddy, G. K.; Boolchand, P.; Smirniotis, P. G. *J. Phys. Chem. C* **2012**, *116*, 11019-11031.
18. Keiski, R. L.; Salmi, T. *Appl. Catal. A: General* **1992**, *87*, 185-203.
19. Natesakhawat, S.; Wang, X.; Zhang, L.; Ozkan, U. S. *J. Mol. Catal. A: Chemical* **2006**, *260*, 82-94.
20. Lee, J. Y.; Lee, D. -.; Hong, Y. -.; Lee, K. -. *Int. J. of Hydrogen Energy* **2011**, *36*, 8173-8180.
21. Martis, V.; Oldman, R.; Anderson, R.; Fowles, M.; Hyde, T.; Smith, R.; Nikitenko, S.; Bras, W.; Sankar, G. *Phys. Chem. Chem. Phys.*, *2013*, *15*, 168 **2013**, *15*, 168-175.
22. Quadro, E. B.; Dias, M. d. L. R.; Maria, A.; Amorim, M.; Rangel, M. d. C. *J. Braz. Chem. Soc.* **1999**, *10*, 51-59.
23. Edwards, M. A.; Whittle, D. M.; Rhodes, C.; Ward, A. M.; Rohan, D.; Shannon, M. D.; Hutchings, G. J.; Kiely, C. J. *Phys. Chem. Chem. Phys.* **2002**, *4*, 3902-3908.
24. Martos, C.; Dufour, J.; Ruiz, A. *Int. J. of Hydrogen Energy* **2009**, *34*, 4475-4481.
25. Khaleel, A.; Shehadi, I.; Al-Shamisi, M. *Coll. Surf. A: Phys. Eng. Aspects* **2010**, *355*, 75-82.
26. Domka, F.; Basinska, A.; Przystajko, W.; Fiedorow, R. *Surf. Technol.* **1984**, *21*, 101-108.
27. Tsokov, P.; Blaskov, V.; Klissurski, D.; Tzolovski, I. *J. Mat. Sci.* **1993**, *28*, 184-188.
28. Rangel, M. d. C.; Sassaki, R. M.; Galembeck, F. *Catal. Lett.* **1995**, *33*, 237-254.
29. Chen, L. S.; Lu, G. L. *J. Mat. Sci.* **1999**, *34*, 4193-4197.
30. Kumar, P.; Idem, R. *Energy & Fuels* **2007**, *21*, 522-529.
31. Scariot, M.; Francisco, M. S. P.; Jordao, M. H.; Zanchet, D.; Logli, M. A.; Vicentini, V. P. *Catal. Today* **2008**, *133-135*, 174-180.

32. Boudjemaa, A.; Auroux, A.; Boumaza, S.; Trari, M.; Cherifi, O.; Bouarab, R. *React. Kinet. Catal. Lett.* **2009**, *98*, 319-325.
33. Reddy, G. K.; Boolchand, P.; Smirniotis, P. G. *J. Catal.* **2011**, *282*, 258-269.
34. Reddy, G. K.; Smirniotis, P. G. *Catal. Lett.* **2011**, *141*, 27-32.
35. Meshkani, F.; Rezaei, M. *J. Ind. Eng. Chem.* **2014**, *20*, 3297-3302.
36. Busca, G.; Lorenzelli, V. *Mat. Chem.* **1980**, *5*, 213-224.
37. Busca, G.; Lorenzelli, V. *React. Kinet. Catal. Lett.* **1980**, *15*, 273-278.
38. Busca, G.; Lorenzelli, V. *J. Catal.* **1980**, *66*, 155-161.
39. Busca, G.; Lorenzelli, V. *Mat. Chem.* **1982**, *7*, 89-126.
40. Lorenzelli, V.; Busca, G.; Sheppard, N.; Al-Mashta, F. *Journal of Molecular Structure* **1982**, *80*, 181-186.
41. Ramis, G.; Busca, G.; Lorenzelli, V. *Mat. Chem. Phys.* **1991**, *29*, 425-435.
42. Busca, G.; Lorenzelli, V.; Ramis, G.; Willey, R. J. *Langmuir* **1993**, *9*, 1492-1499.
43. de Faria, D.; Silva, S.; de Oliveira, M. *J. Raman Spectrosc.* **1997**, *28*, 873-878.
44. Cornell, R. M.; Schwertmann, U. *The Iron Oxides: Structure, Properties, Reactions, Occurences and Uses*; Wiley-VCH Verlag GmbH & Co. KGaA: Weinheim, 2003; , pp 703.
45. Baltrusaitis, J.; Jensen, J. H.; Grassian, V. H. *J. Phys. Chem. B* **2006**, *110*, 12005-12016.
46. de Smit, E.; Weckhuysen, B. M. *Chem. Soc. Rev.* **2008**, *37*, 2758-2781.
47. Boudjemaa, A.; Daniel, C.; Mirodatos, C.; Trari, M.; Auroux, A.; Bouarab, R. *C. R. Chimie* **2011**, *14*, 534-538.
48. Busca, G.; Lorenzelli, V. *J. Chem. Soc. , Faraday Trans.* **1992**, *88*, 2783-2789.
49. Topsoe, H.; Dumesic, J. A.; Boudart, M. *J. Phys. -Paris* **1974**, *35*, 411-413.
50. Cherkezova-Zheleva, Z.; Mitov, I. *J. Physics: Conf. Series* **2010**, *217*, 012044-012047.
51. Zanchet, D.; Rodella, C. B.; Lopes, L. J. S.; Logli, M. A.; Vicentini, V. P.; Wen, W.; Hanson, J. C.; Rodriguez, J. A. *AIP Conf. Proc.* **2009**, *1092*, 25-28.
52. Kendelewicz, T.; Kaya, S.; Newberg, J. T.; Bluhm, H.; Mulakaluri, N.; Moritz, W.; Scheffler, M.; Nilsson, A.; Pentcheva, R.; Brown, G. E. *J. Phys. Chem. C* **2013**, *117*, 2719-2733.

53. Patlolla, A.; Carino, E. V.; Ehrlich, S. N.; Stavitski, E.; Frenkel, A. I. *ACS Catal.* **2012**, *2*, 2216-2223.
54. Boreskov, G. K. *Discuss. Faraday Soc.*, **1966**, *41*, 263-276.
55. Muzykantov, V. S.; Popovskii, V. V.; Boreskov, G. K.; Panov, G. I.; Shkrabina, R. A. *Sov. Appl. Mech.* **1969**, *5*, 344-350.
56. Kasatkina, L. A.; Mekipelov, V. N.; Zhivotenko, N. N. *Kinet. Katal.* **1973**, *14*, 363-371.
57. Udovic, T. J.; Dumesic, J. A. *J. Catal.* **1984**, *89*, 314-326.
58. Lund, C. R. F.; Kubsh, J. E.; Dumesic, J. A. In *Solid State Chemistry in Catalysis*; Grasselli, R. K., Ed.; American Chemical Society: Washington, DC, 1985; Vol. 279, pp 313-338.
59. Rethwisch, D. G.; Dumesic, J. A. *Appl. Catal.* **1986**, *21*, 97-109.
60. Weckhuysen, B. M.; Wachs, I. E. *J. Chem. Soc., Faraday Trans.* **1996**, *92*, 1969-1973.
61. Kubsh, J. E.; Dumesic, J. A. *AIChE J.* **1982**, *28*, 793-800.
62. Tinkle, M.; Dumesic, J. A. *J. Phys Chem.* **1984**, *88*, 4127-4130.
63. Rethwisch, D. G.; Dumesic, J. A. *Langmuir* **1986**, *2*, 73-79.
64. Tinkle, M.; Dumesic, J. A. *J. Catal.* **1987**, *103*, 65-78.
65. Rethwisch, D. G.; Dumesic, J. A. In *Catalytic Activation of Carbon Dioxide*; Ayers, W. M., Ed.; American Chemical Society: Washington, DC, 1988; Vol. 363, pp 102-122.
66. Zhu, M.; Wachs, I. E. *ACS Catalysis* **2016**, *6*, 1764-1767.
67. Boreskov, G. K. *Kinet. Katal.* **1970**, *11*, 374-382.
68. Boreskov, G. K. *Kinet. Katal.* **1980**, *11*, 312.
69. Rethwisch, D. G.; Dumesic, J. A. *J. Phys Chem.* **1986**, *90*, 1625-1630.
70. Oki, S.; Mezaki, R. *J. Phys. Chem.* **1973**, *77*, 1601-1605.
71. Armstrong, E. F.; Hilditch, T. P. In *In A Study of Catalytic Actions at Solid Surfaces. IV. The Interaction of Carbon Monoxide and Steam as Conditioned by Iron Oxide and by Copper*; Proceedings of the Royal Society of London. Series A, Containing Papers of a Mathematical and Physical Character; The Royal Society: London, 1920; Vol. 97, pp 265-273.
72. Mezaki, R.; Oki, S. *J. Catal.* **1973**, *30*, 488-489.
73. Chinchin, G. C.; Logan, R. H.; Spencer, M. S. *Appl. Catal.* **1984**, *12*, 97-103.

74. Chinchin, G. C.; Logan, R. H.; Spencer, M. S. *Appl. Catal.* **1984**, *12*, 69-88.
75. Chinchin, G. C.; Logan, R. H.; Spencer, M. S. *Appl. Catal.* **1984**, *12*, 89-96.
76. Botes, F. G. *Applied Catalysis A: General* **2007**, *328*, 237-242.
77. Vimont, A.; Daturi, M.; Winfield, J. M. In *Functionalized Inorganic Fluorides: Synthesis, Characterizations & Properties of Nanostructured Solids*; Tressaud, E., Ed.; Wiley-Blackwell: Chichester, UK, 2010; Vol. Chap. 4, pp 101-139.
78. Lee, E.; Wachs, I. E. *J. Phys. Chem. C* **2007**, *111*, 14410-14425.
79. Frenkel, A. I.; Wang, Q.; Marinkovic, N.; Chen, J. G.; Barrio, L.; Si, R.; Lopez-Camara, A.; Estrella, A. M.; Rodriguez, J. A.; Hanson, J. C. *J. Phys. Chem. C* **2011**, *115*, 17884-17890.
80. Tao, F. *Chem. Commun.* **2012**, *48*, 3812-3814.
81. Wen, C.; Zhu, Y.; Ye, Y.; Zhang, S.; Cheng, F.; Liu, Y.; Wang, P.; Tao, F. *ACS Nano* **2012**, *6*, 9305-9313.
82. Zhang, S.; Nguyen, L.; Zhu, Y.; Zhan, S.; Tsung, C. -.; Tao, F. *Acc. Chem. Res.* **2013**, *46*, 1731-1739.
83. Hardcastle, F. D.; Wachs, I. E. *J. Mol. Catal.* **1988**, *46*, 173-186.
84. Cieslak-Golonka, M. *Coord. Chem. Rev.* **1991**, *109*, 223-249.
85. Vuurman, M. A.; Wachs, I. E.; Stufkens, D. J.; Oskam, A. *J. Mol. Catal.* **1993**, *80*, 209-227.
86. Kagwade, S. V.; Clayton, C. R.; Halada, G. P. *Surf. Interface Anal.* **2001**, *31*, 442-447.
87. Biesinger, M. C.; Payne, B. P.; Grosvenor, A. P.; Lau, L. W. M.; Gerson, A. R.; Smart, R. S. C. *Appl. Surf. Sci.* **2011**, *257*, 2717-2730.
88. Guo, Q.; Moller, P. J. *Surface Science Letters* **1995**, *340*, L999-L1004.
89. Lemire, C.; Bertarione, S.; Zecchina, A.; Scarano, D.; Chaka, A.; Shaikhutdinov, S.; Freund, H. -. *Physical Review Letters* **2005**, *94*, 166101.
90. Lutz, H. D.; Moller, H.; Schmidt, M. *J. Mol. Struct.* **1994**, *328*, 121-132.
91. Oh, S. J.; Cook, D. C.; Townsend, H. E. *Hyperfine Interactions* **1998**, *112*, 59-66.
92. Frenkel, A. I.; Cross, J. O.; Fanning, D. M.; Robinson, I. K. *J. Synchrotron Rad.* **1999**, *6*, 332-334.
93. Hadjiivanov, K. I.; Vayssilov, G. N. *Adv. Catal.* **2002**, *47*, 307-511.
94. Vimont, A.; Leclerc, H.; Mauge, F.; Daturi, M.; Lavalley, J. C.; Surble, S.; Serre, C.; Ferey, G. J. *Phys. Chem. C* **2007**, *111*, 383-388.



- 1  
2 95. Busca, G.; Lorenzelli, V. *Materials Chemistry* **1982**, 7, 89.  
3  
4 96. Busca, G.; Lamotte, J.; Lavalley, J. C.; Lorenzelli, V. *J. Am. Chem. Soc.* **1987**, 109, 5197-5202.  
5  
6 97. Hadjiivanov, K. I.; Busca, G. *Langmuir* **1994**, 10, 4534-4541.  
7  
8 98. Glisenti, A. *J. Chem. Soc., Faraday Trans.* **1998**, 94, 3671-3676.  
9  
10 99. Landon, J.; Demeter, E.; Inoglu, N.; Keturakis, C.; Wachs, I. E.; Vasic, R.; Frenkel, A. I.; Kitchin, J.  
11 R. *ACS Catal.* **2012**, 2, 1793-1801.  
12  
13 100. Stephens, J. S.; Cruickshank, D. W. J. *Acta Cryst.* **1970**, B26, 222-226.  
14  
15 101. Busca, G. *J. Raman Spectrosc.* **2002**, 33, 348-358.  
16  
17 102. Robbins, M.; Wertheim, G. K.; Sherwood, R. C.; Buchanan, D. N. E. *J. Phys. Chem. Solids* **1971**,  
18 32, 717-729.  
19  
20 103. Sharp, J. C.; Yao, Y. X.; Campbell, C. T. *J. Phys. Chem. C* **2013**, 117, 24932-24936.  
21  
22 104. Joseph, Y.; Kuhrs, C.; Ranke, W.; Ritter, M.; Weiss, W. *Chem. Phys. Lett.* **1999**, 314, 195-202.  
23  
24  
25  
26  
27  
28  
29  
30  
31  
32  
33  
34  
35  
36  
37  
38  
39  
40  
41  
42  
43  
44  
45  
46  
47  
48  
49  
50  
51  
52  
53  
54  
55  
56  
57  
58  
59  
60

